



GJ 3929: High-precision Photometric and Doppler Characterization of an Exo-Venus and Its Hot, Mini-Neptune-mass Companion

Corey Beard¹ , Paul Robertson¹ , Shubham Kanodia^{2,3,4} , Jack Lubin¹ , Caleb I. Cañas^{2,3} , Arvind F. Gupta^{2,3} , Rae Holcomb¹ , Sinclair Jones⁵ , Jessica E. Libby-Roberts^{2,3} , Andrea S. J. Lin^{2,3} , Suvrath Mahadevan^{2,3} , Guðmundur Stefánsson^{6,30} , Chad F. Bender⁷ , Cullen H. Blake⁸ , William D. Cochran⁹ , Michael Endl^{10,11} , Mark Everett¹² , Eric B. Ford^{2,3,13,14} , Connor Fredrick^{15,16} , Samuel Halverson¹⁷ , Leslie Hebb¹⁸ , Dan Li¹⁹ , Sarah E. Logsdon¹⁹ , Jacob Luhn¹ , Michael W. McElwain²⁰ , Andrew J. Metcalfe^{21,22,23} , Joe P. Ninan²⁴ , Jayadev Rajagopal¹⁹ , Arpita Roy^{25,26} , Maria Schutte²⁷ , Christian Schwab²⁸ , Ryan C. Terrien²⁹ , John Wisniewski²⁷ , and Jason T. Wright^{2,3,4}

¹ Department of Physics and Astronomy, 4129 Frederick Reines Hall, University of California, Irvine, Irvine, CA 92697, USA; ccbeard@uci.edu

² Department of Astronomy & Astrophysics, 525 Davey Laboratory, The Pennsylvania State University, University Park, PA 16802, USA

³ Center for Exoplanets and Habitable Worlds, 525 Davey Laboratory, The Pennsylvania State University, University Park, PA 16802, USA

⁴ Penn State Extraterrestrial Intelligence Center, 525 Davey Laboratory, The Pennsylvania State University, University Park, PA 16802, USA

⁵ Princeton University, Department of Astrophysical Sciences, 4 Ivy Lane, Princeton, NJ 08540, USA

⁶ Department of Astrophysical Sciences, Princeton University, 4 Ivy Lane, Princeton, NJ 08540, USA

⁷ Steward Observatory, The University of Arizona, 933 N. Cherry Ave, Tucson, AZ 85721, USA

⁸ Department of Physics and Astronomy, University of Pennsylvania, 209 S. 33rd St., Philadelphia, PA 19104, USA

⁹ McDonald Observatory and Center for Planetary Systems Habitability, The University of Texas, Austin, TX 78712, USA

¹⁰ Center for Planetary Systems Habitability, The University of Texas at Austin, Austin, TX 78712, USA

¹¹ Department of Astronomy, The University of Texas at Austin, TX 78712, USA

¹² National Optical Infrared Astronomy Research Laboratory, 950 N. Cherry Ave., Tucson, AZ 85719, USA

¹³ Institute for Computational and Data Sciences, The Pennsylvania State University, University Park, PA 16802, USA

¹⁴ Center for Astrostatistics, 525 Davey Laboratory, The Pennsylvania State University, University Park, PA 16802, USA

¹⁵ Time and Frequency Division, National Institute of Standards and Technology, 325 Broadway, Boulder, CO 80305, USA

¹⁶ Department of Physics, University of Colorado, 2000 Colorado Avenue, Boulder, CO 80309, USA

¹⁷ Jet Propulsion Laboratory, California Institute of Technology, 4800 Oak Grove Drive, Pasadena, CA 91109, USA

¹⁸ Department of Physics, Hobart and William Smith Colleges, 300 Pulteney Street, Geneva, NY 14456, USA

¹⁹ NSF's National Optical-Infrared Astronomy Research Laboratory, 950 N. Cherry Ave., Tucson, AZ 85719, USA

²⁰ Exoplanets and Stellar Astrophysics Laboratory, NASA Goddard Space Flight Center, Greenbelt, MD 20771, USA

²¹ Space Vehicles Directorate, Air Force Research Laboratory, 3550 Aberdeen Ave. SE, Kirtland AFB, NM 87117, USA

²² Time and Frequency Division, National Institute of Technology, 325 Broadway, Boulder, CO 80305, USA

²³ Department of Physics, 390 UCB, University of Colorado Boulder, Boulder, CO 80309, USA

²⁴ Department of Astronomy and Astrophysics, Tata Institute of Fundamental Research, Homi Bhabha Road, Colaba, Mumbai 400005, India

²⁵ Space Telescope Science Institute, 3700 San Martin Dr., Baltimore, MD 21218, USA

²⁶ Department of Physics and Astronomy, Johns Hopkins University, 3400 N. Charles St., Baltimore, MD 21218, USA

²⁷ Homer L. Dodge Department of Physics and Astronomy, University of Oklahoma, 440 W. Brooks Street, Norman, OK 73019, USA

²⁸ Department of Physics and Astronomy, Macquarie University, Balaclava Road, North Ryde, NSW 2109, Australia

²⁹ Carleton College, One North College St., Northfield, MN 55057, USA

Received 2022 June 3; revised 2022 July 18; accepted 2022 July 21; published 2022 August 30

Abstract

We detail the follow-up and characterization of a transiting exo-Venus identified by TESS, GJ 3929b (TOI-2013b), and its nontransiting companion planet, GJ 3929c (TOI-2013c). GJ 3929b is an Earth-sized exoplanet in its star's Venus zone ($P_b = 2.616272 \pm 0.000005$ days; $S_b = 17.3^{+0.8}_{-0.7} S_{\oplus}$) orbiting a nearby M dwarf. GJ 3929c is most likely a nontransiting sub-Neptune. Using the new, ultraprecise NEID spectrometer on the WIYN 3.5 m Telescope at Kitt Peak National Observatory, we are able to modify the mass constraints of planet b reported in previous works and consequently improve the significance of the mass measurement to almost 4σ confidence ($M_b = 1.75 \pm 0.45 M_{\oplus}$). We further adjust the orbital period of planet c from its alias at 14.30 ± 0.03 days to the likely true period of 15.04 ± 0.03 days, and we adjust its minimum mass to $m \sin i = 5.71 \pm 0.92 M_{\oplus}$. Using the diffuser-assisted ARCTIC imager on the ARC 3.5 m telescope at Apache Point Observatory, in addition to publicly available TESS and LCOGT photometry, we are able to constrain the radius of planet b to $R_p = 1.09 \pm 0.04 R_{\oplus}$. GJ 3929b is a top candidate for transmission spectroscopy in its size regime ($TSM = 14 \pm 4$), and future atmospheric studies of GJ 3929b stand to shed light on the nature of small planets orbiting M dwarfs.

Unified Astronomy Thesaurus concepts: [Exoplanets \(498\)](#); [Mini Neptunes \(1063\)](#); [Super Earths \(1655\)](#); [Transmission spectroscopy \(2133\)](#); [Radial velocity \(1332\)](#); [Transits \(1711\)](#)

³⁰ Henry Norris Russell Fellow.

1. Introduction

Transit photometry has become an extremely important technique for the characterization of exoplanets and has long been the most fruitful method for identifying candidates in the first place (Borucki et al. 2010). With the advent of the Transiting Exoplanet Survey Satellite (TESS; Ricker et al. 2015), we are in a new era of exoplanet detection around low-mass stars. Since the beginning of the TESS mission, over 5000 new exoplanet candidates have been discovered. Many identified candidates are false positives, however, and observations using different techniques are often required to accurately characterize orbital periods, rule out false-positive scenarios, detect longer-period or nontransiting companions, or measure additional parameters of an exoplanet (e.g., Kanodia et al. 2021; Weiss et al. 2021; Cañas et al. 2022; Lubin et al. 2022). Radial velocity (RV) observations are a particularly important follow-up method, as they allow for (1) independent confirmation of a transiting planet signal, (2) characterization of a planet’s mass, and (3) a search for nontransiting companion planets.

A transiting exoplanet candidate with a 2.6-day period was first identified by the TESS Science Processing and Operations Center (SPOC; Jenkins et al. 2016) pipeline around the nearby (15.822 ± 0.006) M dwarf GJ 3929 on 2020 June 19, then designated TOI-2013.01. Our team began follow-up observations using RV instruments and high-contrast imaging shortly after this announcement, with the intent to confirm the planetary nature of this system and refine the planetary parameters of the transiting candidate.

Kemmer et al. (2022) recently published an analysis of the system, placing constraints on its planetary parameters and validating its planetary nature, as well as discovering a second, nontransiting planet candidate during their analysis. Kemmer et al. (2022) were unable to precisely constrain the mass of the transiting planet ($K/\sigma = 2.88$), however, possibly due to the unanticipated existence of planet c.

Using precise RVs obtained with the NEID spectrograph on the WIYN³¹ 3.5 m telescope at Kitt Peak National Observatory (KPNO), RVs taken with the Habitable Zone Planet Finder, and previously published CARMENES RV data, we were able to refine the mass measurements of both planets in the system. Using two ground-based transits obtained with the diffuser-assisted ARCTIC imager, in addition to publicly available TESS and LCOGT data, we refine the radius measurement of this system. Furthermore, our analysis concludes that the additional nontransiting planet candidate has a period of ~ 15 days, and we upgrade GJ 3929c from a candidate to a planet.

In Section 2, we give a summary of the data used in our analysis. In Section 3, we detail our estimation of the system’s stellar parameters. In Section 4, we detail the steps taken to measure planetary and orbital parameters and the investigation of an additional planet. In Section 5, we discuss our findings and the implications for the system. Finally, Section 6 summarizes our results and conclusions.

2. Observations

A summary of our observational data and key properties is given in Table 1.

³¹ The WIYN Observatory is a joint facility of the University of Wisconsin –Madison, Indiana University, NSF’s NOIRLab, the Pennsylvania State University, Purdue University, and the University of California, Irvine.

2.1. TESS

GJ 3929 was observed by the TESS spacecraft between 2020 April 16 and June 8. These dates correspond to Sectors 24 and 25 of the TESS nominal mission. GJ 3929 was observed in CCD 1 of Camera 1 during sector 24 and CCD 2 of Camera 1 during sector 25. The TESS photometry was first reduced by SPOC. After initial processing, we used the pre-search data conditioning simple aperture photometry (PDCSAP; Stumpe et al. 2012) in our analysis. Data points flagged as poor quality are discarded before analysis. A plot of the TESS PDCSAP flux used in the analysis is shown in Figure 1.

2.2. Ground-based Photometric Follow-up

Ground-based follow-up can be a useful tool not only to validate the planetary nature of transiting signals but also to refine the measured parameters of transiting exoplanets. Here we detail the ground-based photometric follow-up for GJ 3929b.

2.2.1. ARCTIC

We observed three transits of GJ 3929b on the nights of 2021 February 26, 2021 April 30, and 2021 September 21, using the Astrophysical Research Consortium (ARC) Telescope Imaging Camera (ARCTIC; Huehnerhoff et al. 2016) at the ARC 3.5 m Telescope at Apache Point Observatory (APO). To achieve precise photometry on nearby bright stars, we used the engineered diffuser described in Stefansson et al. (2017).

The air mass of GJ 3929 varied from 1.00 to 1.66 over the course of its observation on 2021 February 26. The observations were performed using a 30 nm wide narrowband Semrock filter centered at 857 nm (described in Stefansson et al. 2018) owing to moderate cloud coverage, with an exposure time of 33.1 s in the quad-readout mode with 2×2 on-chip binning. In the 2×2 binning mode, ARCTIC has a gain of 2 e/ADU, a plate scale of $0''.228 \text{ pixel}^{-1}$, and a readout time of 2.7 s. We reduced the raw data using *AstroImageJ* (Collins et al. 2017). We selected a photometric aperture of 31 pixels ($7''.07$) and used an annulus with an inner radius of 70 pixels ($15''.96$) and an outer radius of 100 pixels ($22''.8$).

We also observed a transit of GJ 3929b on 2021 April 30. The air mass during observations varied between 1.00 and 1.51. The observations were performed using the same Semrock filter as described previously, with an exposure time of 45 s in the quad-readout mode with 2×2 on-chip binning. For the final reduction, we selected a photometric aperture of 33 pixels ($7''.52$) and used an annulus with an inner radius of 58 pixels ($13''.22$) and an outer radius of 87 pixels ($19''.84$).

We observed a final transit of GJ 3929b on 2021 September 21. The air mass during observations varied between 1.21 and 3.22, and the resulting scatter in data points was >3 times the values of either previous ARCTIC night ($\text{rms}_{20210226} = 1000$ ppm; $\text{rms}_{20210430} = 910$ ppm; $\text{rms}_{20210921} = 3400$ ppm). Consequently, we chose not to use this final ARCTIC transit during analysis of planet b.

We checked for air-mass correlation on each night but found little evidence for any significant correlation. A plot of the ARCTIC transits used in our final analysis is visible in Figure 4.

2.2.2. LCOGT

We additionally use publicly available data taken by the Las Cumbres Observatory Global Telescope Network (LCOGT;

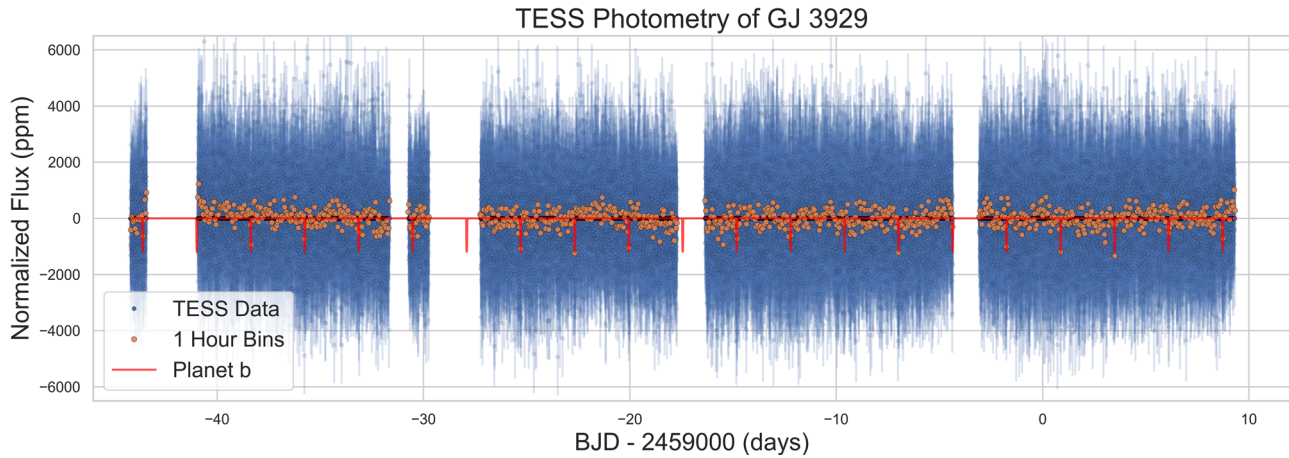


Figure 1. PDCSAP flux of GJ 3929 as taken during TESS Sectors 24 and 25. Overlaid is data binned into 1 hr intervals. Additionally, we plot a maximum a-posteriori (MAP) fit of the transits of planet b. A phase fold of the transits after our complete analysis is visible in Figure 4. The transit model is described in Section 4.1.

Table 1
Summary of Observational Data

Instrument	Date Range	rms	Average Error	Type
TESS	2020 Apr 16–2020 Jun 8	1346 ppm	1441 ppm	Photometry
ARCTIC	2021 Feb 27–2021 Apr 30	1000 ppm	734 ppm	Photometry
LCO	2021 Apr 15	1522 ppm	692 ppm	Photometry
CARMENES	2020 Jul 30–2021 Jul 19	3.87 m s ⁻¹	1.97 m s ⁻¹	RV
HPF	2021 Aug 27–2022 Mar 11	8.81 m s ⁻¹	8.42 m s ⁻¹	RV
NEID	2021 Jan 6–2022 Jan 27	10.6 m s ⁻¹	1.55 m s ⁻¹	RV

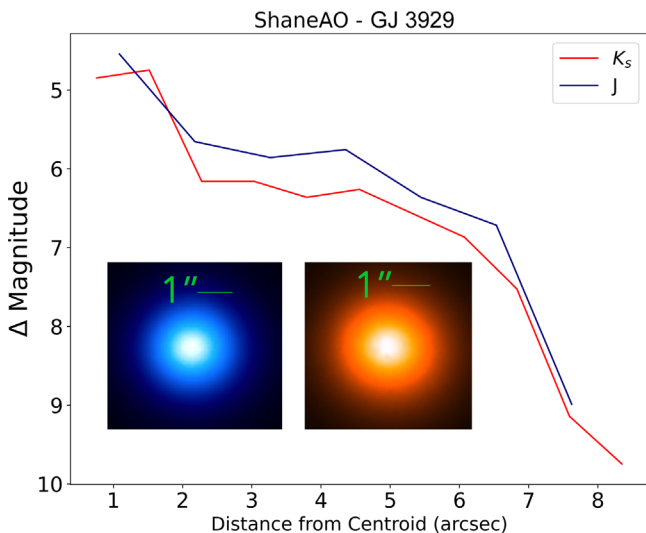


Figure 2. 5σ contrast curves of GJ 3929 taken using the K_s and J filters. The data were taken on 2021 February 26. The overcast conditions and poor seeing on 2021 February 26 resulted in challenges with sky subtraction. As a result, the magnitude difference between the centroid and background does not drop as quickly as expected.

Brown et al. 2013). These data were obtained from the Exoplanet Follow-up Observing Program (ExoFOP) website.³² Two transits of GJ 3929b were obtained using the LCOGT. The first transit was obtained on 2021 April 10. Data were taken by both the SINISTRO CCDs at the 1 m telescopes of the McDonald Observatory (McD) and the Cerro Tololo Inter-

American Observatory (CTIO). Both instruments have a pixel scale of $0.00389 \text{ pixel}^{-1}$ and a field of view (FOV) of 260×260 .

A second transit was obtained on 2021 April 15. These data were taken simultaneously in four different filters (g' , i' , r' , and z_s') with the Multi-color Simultaneous Camera for studying Atmospheres of Transiting exoplanets 3 camera (MuSCAT3; Narita et al. 2020) mounted on the 2 m Faulkes Telescope North at Haleakala Observatory (HAL). It has a pixel scale of $0.0027 \text{ pixel}^{-1}$, corresponding to an FOV of 9.01×9.01 .

As outlined in Kemmer et al. (2022), high air mass caused the CTIO observations to exhibit higher scatter. In fact, both transits on 2021 April 10 exhibit much higher scatter ($\text{rms}_{\text{CTIO}} = 3300 \text{ ppm}$; $\text{rms}_{\text{MCD}} = 2200 \text{ ppm}$) than on 2021 April 15 ($\text{rms}_{\text{gp}} = 1010 \text{ ppm}$; $\text{rms}_{\text{ip}} = 850 \text{ ppm}$; $\text{rms}_{\text{rp}} = 910 \text{ ppm}$; $\text{rms}_{\text{zs}} = 920 \text{ ppm}$). Consequently, for the same reasons outlined in Section 2.2.1, we chose not to utilize either transit from 2021 April 10 in our final analysis.

The publicly available data were calibrated by the LCOGT BANZAI pipeline (McCully et al. 2018), and photometric data were extracted using AstroImageJ (Collins et al. 2017). The resulting photometric data are the same as those that were utilized in Kemmer et al. (2022).

2.3. High-contrast Imaging

High-contrast imaging can be important for ruling out false-positive scenarios. Kemmer et al. (2022) used high-resolution images obtained from the AstraLux camera (Hormuth et al. 2008) at the Calar Alto Observatory to rule out false-positive scenarios. They were able to rule out nearby luminous sources down to a $\Delta z' < 5.5$ at $1''$. Here we detail our team's adaptive

³² <https://exofop.ipac.caltech.edu/tess/>

optics (AO) follow-up of GJ 3929b and add to the evidence of a planetary explanation for the transit events.

2.3.1. ShARCS on the Shane Telescope

We observed GJ 3929 using the ShARCS camera on the Shane 3 m telescope at Lick Observatory (Srinath et al. 2014). GJ 3929 was observed using the K_S and J filters on the night of 2021 February 26. Instrument repairs prevented our observations from benefiting from Laser Guide Star (LGS) mode. Fortunately, GJ 3929 is sufficiently bright that LGS mode is helpful but not necessary. Further instrument repairs prevented our observations from using a dither routine to create master-sky images of GJ 3929. Instead, after a series of observations, we shifted several arcseconds to an empty region of sky and took images with the same exposure time for purposes of sky subtraction.

The raw data are reduced using a custom pipeline developed by our team (described in Beard et al. 2022). Using algorithms from Espinoza et al. (2016), we then generate a 5σ contrast curve as the final part of our analysis (Figure 2). We detect no companions at a $\Delta K_S = 4.85$ at $0''.76$ and $\Delta K_S = 9.75$ at $8''.35$. Additionally, we detect no companions at $\Delta J = 4.54$ at $1''.09$ and $\Delta J = 7.62$ at $8''.99$.

We note that observing conditions on 26 February 2021 were marginal. As a result of overcast conditions and poor seeing, the FWHM of the centroid in each reduced AO image was fairly large ($0''.77$ and $1''.11$). Consequently, our final constraints on nearby luminous companions are not as tight as they might have been. However, our high-contrast images were taken in redder wave bands than the z' filter used in Kemmer et al. (2022), and so we provide additional sensitivity toward detecting redder, cooler companions. In tandem, our results and those outlined in Kemmer et al. (2022) are consistent: we detect no nearby luminous companions as an explanation for the observed transit event.

2.4. Radial Velocity Follow-up

We obtained RVs of GJ 3929b in order to constrain the mass of the system and to independently confirm the planetary nature of the transiting planet. Here we detail the RV data acquired for the system GJ 3929.

2.4.1. The NEID Spectrometer on the WIYN 3.5 m Telescope at KPNO

We obtained RVs of GJ 3929 using the new, ultraprecise NEID spectrometer (Schwab et al. 2016) on the WIYN 3.5 m telescope at KPNO. NEID is an environmentally stabilized (Stefansson et al. 2016; Robertson et al. 2019) fiber-fed spectrograph (Kanodia et al. 2018) with broad wavelength coverage (3800–9300 Å). We observed GJ 3929 in High Resolution (HR) mode with an average resolving power $\mathcal{R} = 110,000$. The default NEID pipeline utilizes the cross-correlation function (CCF; Baranne et al. 1996) method to produce RVs. However, this method tends to be less effective on M dwarfs (e.g., Anglada-Escudé et al. 2012), and so we use a modified version of the SpEctrum Radial Velocity AnaLyser pipeline (SERVAL; Zechmeister et al. 2018) as described in Stefansson et al. (2021). SERVAL shifts and combines all observed spectra into a master template and compares this template with known reference spectra. We then minimize the χ^2 statistic to determine the shifts of each observed spectrum. We mask telluric and sky emission lines

during this process. A telluric mask is calculated based on their predicted locations using `telfit` (Gullikson et al. 2014), a Python wrapper to the Line-by-Line Radiative Transfer Model package (Clough et al. 2005).

We obtained 27 observations of GJ 3929 between 2021 January 6 and 2022 January 27. Our first two nights of observation for this system used three consecutive 900 s exposures, but we later changed our observation strategy to one 1800 s exposure per night. We obtained a median signal-to-noise ratio (S/N) of 44.8 in order 102 ($\lambda = 4942$ Å) of NEID for each unbinned observation. The median unbinned RV error bar is 1.18 m s⁻¹. The error bars are estimated from expected photon noise. A total of 23 nightly binned RVs were obtained, though four were discarded because the laser frequency comb calibrator was not available on those nights, resulting in a less precise instrument drift solution that is insufficient for precision RV analysis. This left us with 19 nightly binned NEID RVs that were used in the analysis.

2.4.2. The Habitable Zone Planet Finder at McDonald Observatory

We observed GJ 3929 with the Habitable Zone Planet Finder (HPF; Mahadevan et al. 2012, 2014), a near-infrared (NIR; 8080–12780 Å), high-precision RV spectrograph. HPF is located at the 10 m Hobby–Eberly Telescope (HET) in Texas. HET is a fixed-altitude telescope with a roving pupil design. Observations on the HET are queue scheduled, with all observations executed by the HET resident astronomers (Shetrone et al. 2007). HPF is fiber-fed, with separate science, sky, and simultaneous calibration fibers (Kanodia et al. 2018), and has precise, millikelvin-level thermal stability (Stefansson et al. 2016).

We extracted precise RVs with HPF using the modified version of SERVAL Zechmeister et al. (2018) optimized for use for HPF data as described in detail in Stefansson et al. (2020). The RV reduction followed similar steps to those outlined in Section 2.4.1.

We obtained 18 observations of GJ 3929 with HPF over the course of six observing nights. These data were taken between 2021 August 27 and 2022 March 11. We obtained three consecutive exposures on each observing night, resulting in a median unbinned RV error of 7.15 m s⁻¹. Data taken on BJD = 2,459,649 were excluded from our analysis owing to poor weather conditions. Our data set then consists of five nightly binned HPF RVs. Due to the small quantity of the HPF data, we considered fits that did not utilize HPF data. We found that model results did not differ meaningfully whether HPF data were utilized or not, and we include them in our final model for completeness. HPF spectra were still used to derive stellar parameters, as outlined in Section 3.

2.4.3. CARMENES RVs

Our RV modeling also utilizes CARMENES RVs published in Kemmer et al. (2022). Kemmer et al. (2022) published 78 high-precision RVs as a part of their study of GJ 3929 using the CARMENES spectrograph (Quirrenbach et al. 2014). CARMENES is a dual-channel spectrograph with visible and NIR arms ($\mathcal{R}_{\text{VIS}} = 94,600$; $\mathcal{R}_{\text{NIR}} = 80,400$). CARMENES is located at the Calar Alto Observatory in Almería, Spain. RVs of GJ 3929 were taken between 2020 July 30 and 2021 July 19. Each observation lasted 30 minutes, with a median observation S/N of 74. Five RVs were discarded owing to a missing drift

correction in Kemmer et al. (2022), and we do so as well. This results in a final data set containing 73 RVs. These RVs were taken using the visible arm of CARMENES and have a median uncertainty of 1.9 m s^{-1} .

3. Stellar Parameters

We followed steps outlined in Stefánsson et al. (2020) and Beard et al. (2022) to estimate T_{eff} , $\log g$, and $[\text{Fe}/\text{H}]$ values of GJ 3929. The HPF-SpecMatch code is based on the SpecMatch-Emp algorithm from Yee et al. (2017) and compares the high-resolution HPF spectrum of the target star of interest to a library of high-S/N as-observed HPF spectra. This library consists of slowly rotating reference stars with well-characterized stellar parameters from Yee et al. (2017) and an expanded selection of stars from Mann et al. (2015) in the lower effective temperature range. Our analysis was run on 2022 March 3, and the library contained 166 stars during our run.

We shift the observed target spectrum to a library wavelength scale and rank all of the targets in the library using a χ^2 goodness-of-fit metric. After this initial χ^2 minimization step, we pick the five best-matching reference spectra. We then construct a weighted spectrum using their linear combination to better match the target spectrum. A weight is assigned to each of the five spectra according to its goodness of fit. We then assign the target stellar parameter T_{eff} , $\log g$, and $[\text{Fe}/\text{H}]$ values as the weighted average of the five best stars using the best-fit weight coefficients. The final parameters are listed in Table 2. These parameters were derived from the HPF order spanning 8670–8750 Å, as this order is cleanest of telluric contamination. We artificially broadened the library spectra with a $\nu \sin i$ broadening kernel (Gray et al. 1992) to match the rotational broadening of the target star. We determined GJ 3929 to have a $\nu \sin i$ broadening value of $<2 \text{ km s}^{-1}$.

We used EXOFASTv2 (Eastman et al. 2013) to model the spectral energy distributions (SEDs) of GJ 3929 and to derive model-dependent constraints on the stellar mass, radius, and age. EXOFASTv2 utilizes the BT-NextGen stellar atmospheric models (Allard et al. 2012) during SED fits. Gaussian priors were used for the 2MASS (*JHK*), Johnson (*BV*), and Wide-field Infrared Survey Explorer (WISE) magnitudes (W1, W2, W3, and W4; Wright et al. 2010). Our spectroscopically derived host star effective temperature, surface gravity, and metallicity were used as priors during the SED fits as well, and the estimates from Bailer-Jones et al. (2021) were used as priors for distance. We further include in our priors estimates of Galactic dust by Green et al. (2019) to estimate the visual extinction, though we emphasize that this is a conservative upper limit: GJ 3929 is fairly close to Earth and is likely to be foreground to much of the dust utilized in this estimate. We convert this upper limit to a visual magnitude extinction using the $R_v = 3.1$ reddening law from Fitzpatrick (1999). Our final model results are consistent with those derived in Kemmer et al. (2022) and are visible in Table 2.

4. Analysis

Both photometry and RV data were essential for characterizing GJ 3929, as the system may have two or more planets, though we have only detected transits of planet b. First, in Section 4.1, we investigate the transiting planet using our photometric data. Next, we analyze the RV data of GJ 3929 in Section 4.2. Then, we search for additional transiting signals. Finally, in Section 4.5, we combine both data sets to reach our final conclusion.

4.1. Transit Analysis

A 2.6-day transit signal was originally identified by the MIT SPOC pipeline on 2020 June 19, then designated TOI-2013.01. Subsequently, Kemmer et al. (2022) confirmed the planetary nature of the signal in early 2022. We combine the TESS data with our follow-up transits in addition to other publicly available photometric data (detailed in Section 2.2) to further refine the measured parameters of the system.

4.1.1. Modeling the Photometry

We modeled GJ 3929’s photometry using the exoplanet software package (Foreman-Mackey et al. 2021a). First, we downloaded the TESS PDCSAP flux using lightcurve (Lightcurve Collaboration et al. 2018). We then performed a standard quality-flag filter, removing data points designated as of poor quality by the SPOC pipeline, and we median-normalized the TESS data. We then combined the TESS data with our normalized ARCTIC and LCOGT data for joint analysis.

Initial fits to ARCTIC and LCOGT data appeared to have a slight residual trend, and so in our adopted fit we detrended ARCTIC and LCOGT photometry before combining the data sets. We utilized the NumPy polyfit function to fit a line for purposes of detrending (Harris et al. 2020). This function performs a simple least-squares minimization to estimate the linear trend. This detrending was performed before modeling the data, as we found that including a detrending term in the model did not meaningfully improve our results, while increasing the complexity of our model.

We found it best to partition the photometric data into four regions of interest: the TESS data (which consist of two consecutive sectors), two different nights of ARCTIC data, and a night of LCOGT data. Due to the possibility of systematic offsets between nights and the distinct conditions during each night of ARCTIC observations, we choose to treat each ARCTIC night separately in our model. Furthermore, the LCOGT data were taken with four different filters. Consequently, we model each filter separately. For each instrument–filter combination, then, we adopt a unique mean and jitter term. The mean terms are additive offsets to account for potential systematic shifts between nights and are simply subtracted from all data points when fitting. The jitter terms are meant to model additional white noise not properly accounted for in the error bars of the data set and are added in quadrature with the error bars. Our model thus consists of seven total mean terms and seven jitter terms.

The physical transit model was generated using exoplanet functions and the stary light-curve package (Luger et al. 2019), which models the period, transit time, stellar radius, stellar mass, eccentricity, radius, and impact parameter to produce a simulated light curve. We adopt quadratic limb-darkening terms to account for the change in flux that occurs when a planet approaches the limb of a star (Kipping 2013). The two ARCTIC transits were taken using the same Semrock filter, and so we expect their limb-darkening behavior to be the same. Thus, we adopt the same limb-darkening parameters for each ARCTIC transit. We adopt distinct limb-darkening terms for the LCOGT data taken with the SDSS g' , i' , r' , and z_s' filters. We note that this results in six pairs of limb-darkening terms, in contrast to seven separate jitter and mean terms, but is physically motivated.

Table 2
Summary of Stellar Parameters for GJ 3929

Parameter	Description	Value	Reference
Main Identifiers:			
TOI	TESS Object of Interest	2013	TESS mission
TIC	TESS Input Catalogue	188589164	TICv8
GJ	Gliese-Jahreiss Nearby Stars	3929	Gliese-Jahreiss
2MASS	...	J15581883 + 3524236	2MASS
Gaia DR3	...	1372215976327300480	Gaia DR3
Equatorial Coordinates, Proper Motion and Spectral Type:			
α_{J2000}	R.A. (R.A.; deg)	239.57754339(4)	Gaia DR3
δ_{J2000}	Decl. (decl.; deg)	35.40815826(2)	Gaia DR3
μ_α	Proper motion (RA; mas/yr)	-143.28 ± 0.07	TICv8
μ_δ	Proper motion (decl.; mas/yr)	318.22 ± 0.08	TICv8
d	Distance (pc)	15.8 ± 0.02	Bailer-Jones
Optical and NIR magnitudes:			
B	Johnson B mag	14.333 ± 0.008	TICv8
V	Johnson V mag	12.67 ± 0.02	TICv8
g'	Sloan g' mag	15.161 ± 0.006	TICv8
r'	Sloan r' mag	12.2405 ± 0.0009	TICv8
i'	Sloan i' mag	10.921 ± 0.001	TICv8
T	TESS magnitude	10.270 ± 0.007	TICv8
J	J mag	8.69 ± 0.02	TICv8
H	H mag	8.10 ± 0.02	TICv8
K_s	K_s mag	7.87 ± 0.02	TICv8
$W1$	WISE1 mag	7.68 ± 0.02	WISE
$W2$	WISE2 mag	7.54 ± 0.02	WISE
$W3$	WISE3 mag	7.42 ± 0.02	WISE
$W4$	WISE4 mag	7.27 ± 0.08	WISE
Spectroscopic Parameters^a:			
T_{eff}	Effective temperature in K	3384 ± 88	This work
[Fe/H]	Metallicity in dex	-0.02 ± 0.12	This work
$\log(g)$	Surface gravity (cm s^{-2})	4.89 ± 0.05	This work
Model-dependent Stellar SED and Isochrone fit Parameters^b:			
M_*	Mass (M_\odot)	$0.313^{+0.027}_{-0.022}$	This work
R_*	Radius (R_\odot)	0.32 ± 0.01	This work
L_*	Luminosity (L_\odot)	$0.0109^{+0.0005}_{-0.0004}$	This work
ρ_*	Density (g cm^{-3})	13.3 ± 1.1	This work
Age	Age (Gyr)	$7.1^{+4.1}_{-4.9}$	This work
A_v	Visual extinction (mag)	0.005 ± 0.003	This work
d	Distance (pc)	15.822 ± 0.006	This work
Other Stellar Parameters:			
$v \sin i_*$	Rotational velocity (km s^{-1})	< 2	This work
ΔRV	“Absolute” radial velocity (km s^{-1})	10.265 ± 0.008	This work
U, V, W	Galactic velocities (km s^{-1})	$-21.05 \pm 0.04, 10.85 \pm 0.06, 14.66 \pm 0.08$	Kemmer

Note.

^a Derived using the HPF spectral matching algorithm from Stefánsson et al. (2020).

References. TICv8 (Stassun et al. 2018), 2MASS (Cutri et al. 2003), Gaia DR3 (Gaia Collaboration et al. 2022j, in preparation), Bailer-Jones (Bailer-Jones et al. 2018), WISE (Wright et al. 2010), Kemmer (Kemmer et al. 2022).

Similar to Kemmer et al. (2022), we choose not to include a dilution term in our final model. GJ 3929 does not have many neighbors and is much brighter than all of them (Figure 3). GJ 3929 has an estimated contamination ratio of 0.000765, meaning that 0.08% of its flux is possibly from nearby sources (Stassun et al. 2019). This suggests that a dilution term is not necessary.

4.1.2. Inference

After constructing a physical transit model using `starry`, we compare it to the data after it has been adjusted to account for offsets, and we add our jitter parameters in quadrature with

the error bars during likelihood estimation. Each free parameter is given a broad prior to prevent any biasing of the model, and we summarize the priors used in Table 4. The model is then optimized using `scipy.optimize.minimize` (Virtanen et al. 2020), which utilizes the Powell optimization algorithm (Powell 1998). This optimization provides a starting guess for posterior inference. We then used a Markov Chain Monte Carlo (MCMC) sampler to explore the posterior space of each model parameter. `exoplanet` uses the Hamiltonian Monte Carlo (HMC) algorithm with a No U-Turn Sampler (NUTS) for increased sampling efficiency (Hoffman & Gelman 2011). We ran 10,000 tuning steps and 10,000 subsequent steps and

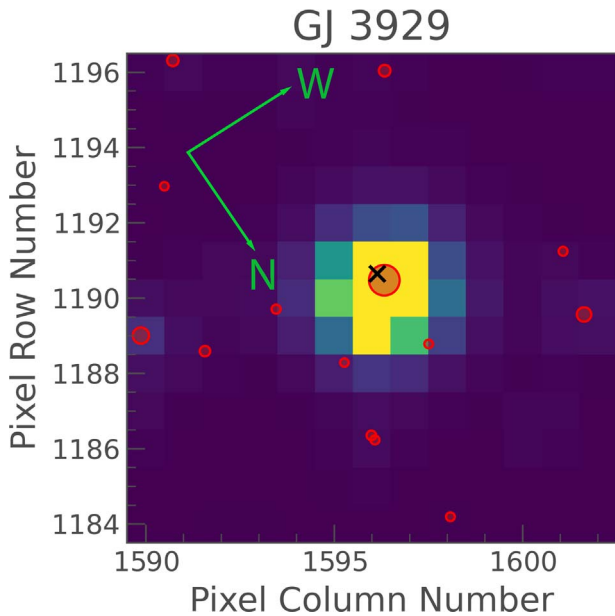


Figure 3. TESS pixel image of GJ 3929 taken during Sector 24, created using the `eleanor` software package (Feinstein et al. 2019). The TICv8 position of GJ 3929 is indicated by a black cross. Red circles correspond to Gaia resolved sources (Gaia Collaboration et al. 2018), with size corresponding to brightness. Because GJ 3929 does not have any bright neighbors, we do not use a dilution term.

assessed convergence criteria using the Gelman–Rubin (G-R) statistic (Ford 2006). We considered a chain well mixed if the G-R statistic was within 1% of unity. All the parameters in our model indicated convergence using this metric.

Our photometry-only fits are consistent with the joint fits adopted in Section 4.5. A final plot of the photometry, folded to the period of planet b, is visible in Figure 4.

4.2. Radial Velocity Analysis

4.2.1. Periodogram Analysis

We first used a Generalized Lomb–Scargle (GLS) periodogram (Zechmeister & Kürster 2009) to analyze the RVs of GJ 3929 and to identify any periodic signals. We estimate the analytical false-alarm levels and normalize the periodogram following the steps outlined in Zechmeister & Kürster (2009), which assume Gaussian noise. With this assumption, we scale the sample variance (and false-alarm levels) by $\frac{N-1}{2}$ in order to reproduce the population variance, which is the quantity of interest in our analysis. Consistent with Kemmer et al. (2022), we detected significant periodicities between 14 and 16 days. In contrast to Kemmer et al. (2022), however, we find that when including the new, more precise NEID RVs (median CARMENES RV error $\sim 1.6\times$ median NEID RV error), as well as our HPF RVs, the 15-day signal has grown in power relative to the 14-day signal, suggesting that it might be the true signal. Relative peak strengths of alias frequencies in a periodogram do not always indicate the true period, however, and we detail a more formal model comparison later in the section. A plot of the combined data set periodogram and periodograms on NEID and CARMENES only are visible in Figure 5. After the subtraction of the longer-period planet c, the signal of the 2.6-day planet b is clearly identifiable in the periodogram.

4.2.2. Modeling the RVs

We used the `RadVel` software package to analyze the RVs of GJ 3929 (Fulton et al. 2018). `RadVel` models an exoplanet’s orbit by solving Kepler’s equation using an iterative method outlined in Danby (1988). Each planetary orbit is then modeled by five fundamental parameters: the planet’s orbital period (P), the planet’s time of inferior conjunction (T_c), the eccentricity of the orbit (e), the argument of periastron (ω), and the velocity semi-amplitude (K). We additionally include instrumental terms, γ and σ , which account for systematic offsets between instruments and excess white noise.

We construct the RV model in a Bayesian context, encoding prior information about each parameter as a part of the model. Similar to the fits described in Section 4.1, we adopt broad priors on the free parameters of our model to prevent any bias in our results, the primary exception being that during RV-only fits we put tight priors on P_b and $T_{\text{con},b}$, as these are much more tightly constrained by transits than by RV fits. We emphasize, however, that our final adopted fit is a joint fit between RVs and transits, detailed in Section 4.5. Detailed prior information is available in Table 4.

4.2.3. Inference

In order to estimate the posterior probability of our model, we used an MCMC sampler to explore the posterior parameter space. `RadVel` utilizes the MCMC sampler outlined in Foreman-Mackey et al. (2013). We first used the Powell optimization method to provide an initial starting guess for each parameter (Powell 1998). We then ran 150 independent chains and assessed convergence using the Gelman–Rubin (G-R) statistic (Ford 2006). The sampling was terminated when the chains were sufficiently mixed. Chains are considered well mixed when the G-R statistic for each parameter is < 1.03 , the minimum autocorrelation time factor is ≥ 75 , the maximum relative change in autocorrelation time is ≤ 0.01 , and there are ≥ 1000 independent draws. All of our considered models eventually satisfied these conditions.

We additionally considered the inclusion of a Gaussian process (GP; Ambikasaran et al. 2015) model to account for coherent stellar activity. Kemmer et al. (2022) identify a rotation period of ~ 120 days for GJ 3929. This value is derived from a combination of long-term photometry taken using the Hungarian Automated Telescope Network (HATNet; Bakos et al. 2004), the All-Sky Automated Search for SuperNovae (ASAS-SN; Shappee et al. 2014), and Joan Oró Telescope (TJO; Colomé et al. 2010) and periodogram analysis of the CARMENES $H\alpha$ values. We use the combined $H\alpha$ values from CARMENES and NEID to expand on this, plotted in Figure 6. While the maximum power occurs at a slightly shorter period than observed in Kemmer et al. (2022), we note that rotational variability is often quasi-periodic in nature and periodograms can have trouble distinguishing longer periods (Lubin et al. 2021). Our value observed here is still consistent with the previously reported value, and we make no amendment to the system’s rotation period.

The >100 -day rotation period of this system is consistent with a quiet, slowly rotating star, and we normally would not expect a large RV signal due to activity. However, Kemmer et al. (2022) found an RV fit that included a GP to be preferred to an RV-only fit, and so we proceed with a series of fits, some of which include

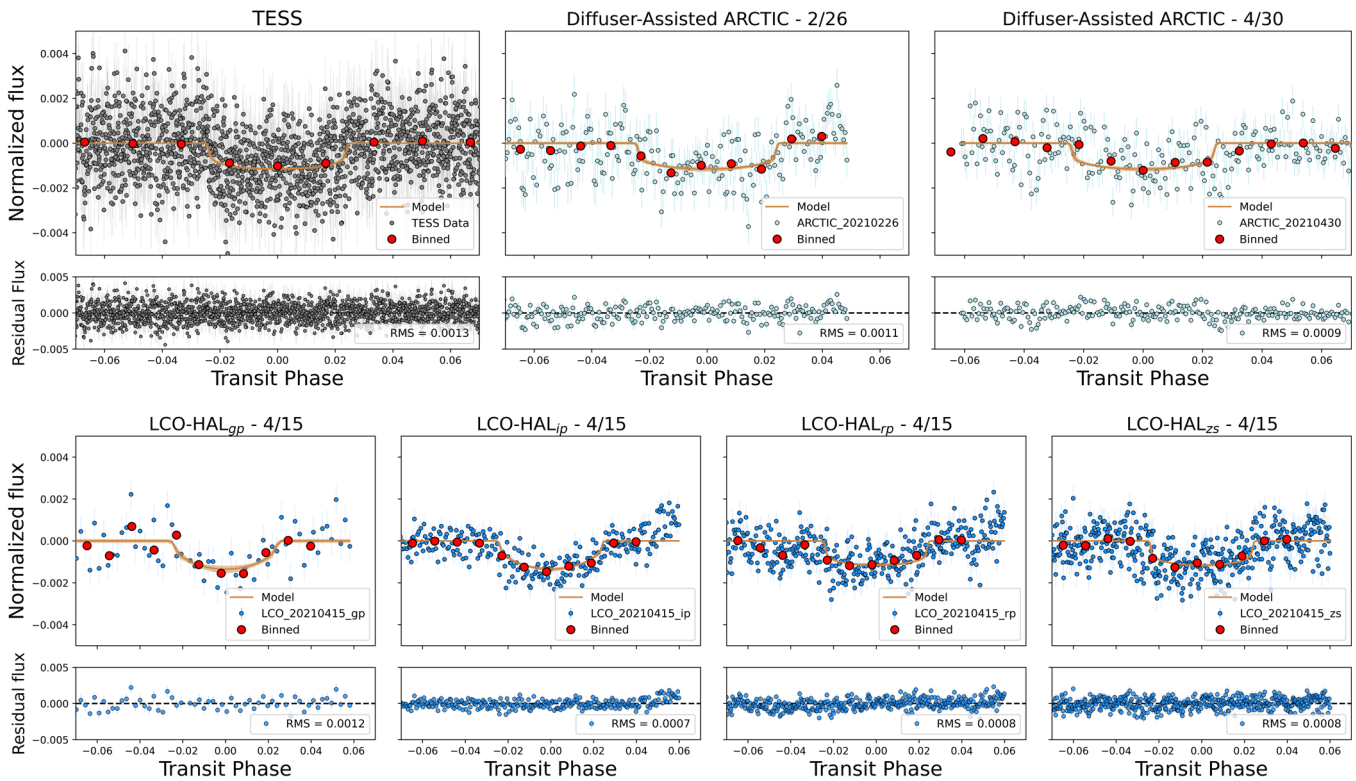


Figure 4. Phase-folded transit fits to TESS data, ARCTIC data, and LCOGT data. We separate the 2021 April 15 transit taken with LCOGT by filter and label them accordingly. Using all of these data allows us to modify previous radius estimates of GJ 3929b.

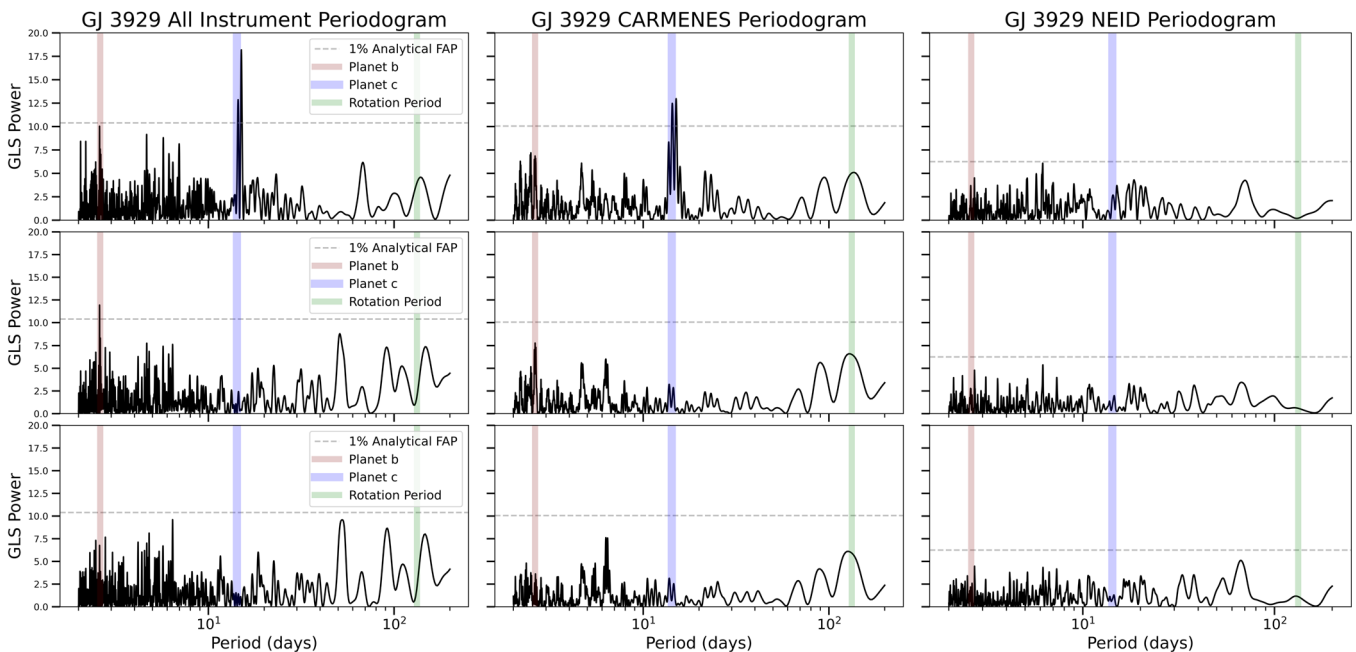


Figure 5. Top: GLS periodograms of the combined data set consisting of NEID, CARMENES, and HPF RVs, CARMENES data only, and NEID data only. Data have been adjusted for offsets. Middle: data after the subtraction of planet c, assuming the values derived in our final posterior fits. Bottom: GLS periodograms of data after the subtraction of planet b and planet c. We do not include a periodogram of HPF-only data owing to its sparseness.

a GP. Our GP fits utilize the quasi-periodic GP kernel owing to its flexibility and wide application in exoplanet astrophysics (e.g., Haywood et al. 2014; López-Morales et al. 2016).

We also compared fits with the GP kernel that was adopted in Kemmer et al. (2022). Kemmer et al. (2022) utilized a combination of two simple harmonic oscillator (SHO;

Foreman-Mackey 2018) kernels, outlined in more detail in Kossakowski et al. (2021). We refer to this as the double simple harmonic oscillator kernel (dSHO).

In order to explore the possibility of an additional planet in the GJ 3929 system and the plausibility of stellar activity interfering with RV signals, we perform a model comparison. Model

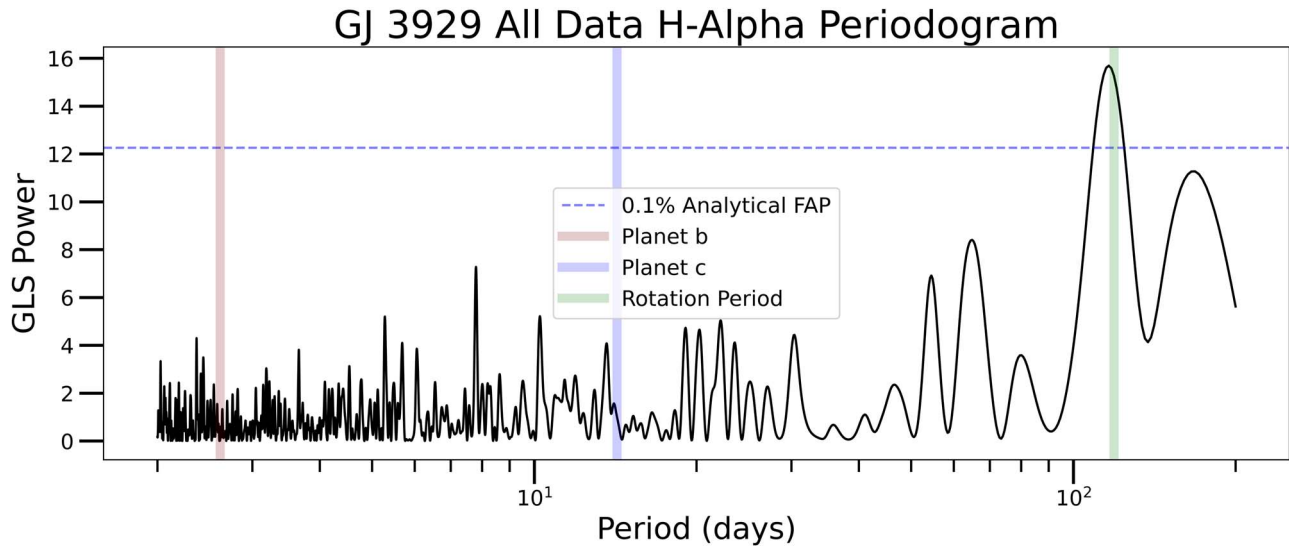


Figure 6. GLS periodogram of the H α data taken by the CARMENES and NEID spectrographs. The only significant signal is at 116 days, which is most likely associated with the stellar rotation period identified in Kemmer et al. (2022). Neither of the planetary periods has any significant power in these data. We do not include HPF, as its bandpass does not include the H α indicator.

comparisons vary in the number of planets included, whether or not we include a GP to account for stellar noise and eccentric fits, and whether or not the second planet is modeled as the 14-day signal or the 15-day signal. A full table of our model results is provided in Table 3. Our analysis found that both the quasi-periodic and dSHO GPs perform similarly in model comparison, and so we only include the quasi-periodic results for brevity. When comparing models, we use the Bayesian information criterion (BIC; Kass & Raftery 1995) and the corrected Akaike information criterion (AICc; Hurvich & Tsai 1993). The BIC of each model can be used to estimate the Bayes factor (BF), a measure of preference for one model over another. Half the difference in BIC between two models is used to estimate the Schwarz criterion, which itself is an approximation of the log BF. The AICc is an approximation of the Kullback–Leibler information, another metric for ranking the quality of models (Hurvich & Tsai 1993).

Kass & Raftery (1995) suggest that a $\log_{10} \text{BF} > 2$ (In $\text{BF} > 4.6$) is decisive evidence for one model over another. For GJ 3929, our two-planet (~ 15 days) model is preferred over the next best model, a two-planet GP (~ 15 days), with a BF of 5.86 (RadVel estimates likelihoods using \ln), suggesting a strong preference for the no-GP case. The AICc simply prefers the model that minimizes the AICc, which is also the two-planet model (~ 15 days). Both methods of estimation are only asymptotically correct, but they are preferred by a wide enough margin and agree with one another. Consequently, we use these comparisons to justify selecting the two-planet model (~ 15 days) without a GP as our best model.

A phase folded diagram of the RV model taken from our final joint fit is included in Figure 7.

4.3. An Additional Transiting Planet?

As elaborated further in Section 4.2 and detailed in Kemmer et al. (2022), GJ 3929 RVs show two strong periodicities between 14 and 16 days. Consistent with Kemmer et al. (2022), fitting either signal eliminates the other, suggesting that one is an alias of the other. Thus, we conclude that the two signals originate from a single source, though the true periodicity is originally unclear. Such a signal might be an additional planet, and if so, it may be transiting. Here we search the TESS

Table 3
RV Model Comparisons^a

Fit	Number of Free Parameters	BIC	AICc
0 planet	4	566.5757	552.0607
...			
1 planet	7	569.5241	548.4207
1 planet ecc	9	578.4362	553.4362
1 planet GP	11	574.0880	545.0023
...			
2 planet (~ 14 day)	10	560.2770	533.0948
2 planet (~ 14 days) ecc (b)	12	567.0928	536.1688
2 planet (~ 14 days) ecc (c)	12	562.6540	531.7300
2 planet (~ 14 days) ecc (both)	14	567.6228	533.2274
2 planet GP (~ 14 days)	14	576.62	542.2246
2 planet (~ 15 days)	10	545.5826	518.4004
2 planet (~ 15 days) ecc (b)	12	552.2589	521.3349
2 planet (~ 15 days) ecc (c)	12	551.8569	520.9229
2 planet (~ 15 days) ecc (both)	14	560.8289	525.8289
2 planet GP (~ 15 days)	14	557.3132	522.9178

Note.

^a Model comparison was performed on RV-only fits. This is motivated in Section 4.5.

photometry for signs of additional transiting exoplanets, with a particular emphasis on planets in this period range.

We use the `TransitLeastSquares` (TLS; Hippke & Heller 2019) Python package in order to search for additional periodic transit signals in the TESS light curves. Unlike a box-fitting least-squares (BLS) algorithm (Kovács et al. 2002), which is used frequently in transit searches, the TLS adopts a more realistic transit shape, increasing its sensitivity to transiting exoplanets, especially smaller ones. Initially, we recover GJ 3929b with a signal detection efficiency (SDE) > 35 , a highly significant detection. Dressing & Charbonneau (2015) suggest that an SDE > 6 represents a conservative cutoff for a “significant” signal, though others adopt higher values (Siverd et al. 2012; Livingston et al. 2018). We then mask the transits of planet b and continue the investigation. Our second check highlights a significant signal

at 13.9 days (SDE = 12.74), somewhat close to the suspected planetary signals from the RVs. However, analysis of the candidate transit event itself seems inconsistent. Using the nonparametric mass–radius relationship from `mrexo` (Kanodia et al. 2019), we estimate that planet c would have a radius of $2.26 R_{\oplus}$ using the minimum mass, and consequently a nongrazing transit depth of 4.19 ppt, more than 4 times as large as planet b. We caution that such mass–radius relationships are associated with a large uncertainty, though Figure 9 makes it clear that GJ 3929c should at least be larger than planet b. However, this “transit” observed by TLS at ~ 14 days has a depth of 0.24 ppt. It is possible that the transits of this candidate are grazing, resulting in an anomalously small transit depth. However, the durations of the transits of this signal are also much longer than expected, at 0.42 days. This not only is inconsistent with a grazing transit but also would be too long for any transit at this period. Finally, the estimated transit phase is totally inconsistent with the time of conjunction found in Kemmer et al. (2022). TLS finds a $T_c = 2,459,867$ BJD, while Kemmer et al. (2022) would have expected a $T_c = 2,459,872$ BJD (scaling back the time of conjunction reported). We thus conclude that this significant ~ 14 -day periodicity identified by the TLS package is not planet c and is most likely noise.

It is possible that planet c is transiting, but that its transits fell into TESS data gaps. In Figure 8, we highlight where the transits of planet c would occur relative to the TESS photometry. We identify no clear transit signals in the data.

We calculate 3σ and 5σ transit windows in Figure 8 by using our posterior period and time of conjunction values for planet c and back-propagating them using standard propagation of error. Consequently, from Figure 8, we can rule out nongrazing transits of planet c with 3σ confidence.

4.4. Candidate Planet, or Planet?

Kemmer et al. (2022) designated the 14-to-15-day signal a planet candidate. While no transit signal is clearly detected at this period, we can rule out most false-positive scenarios.

GJ 3929c might be a highly inclined binary or brown dwarf. While such a scenario cannot easily be ruled out, GJ 3929 has a Gaia RUWE value of 1.185, which is consistent with little astrometric motion (Gaia Collaboration et al. 2016, 2021; Lindegren & Dravins 2021). This suggests that a highly inclined binary scenario is unlikely.

Periodic or quasi-periodic RV signals can also be created by stellar magnetic activity. Our model comparison (Table 3) does not prefer a model that includes activity mitigation, and TESS photometry does not exhibit any obvious periodic variability (Figure 1). Furthermore, no strong signal near 14 or 15 days exists in the $H\alpha$ indicator data (Figure 6). The candidate rotation period does show up very strongly in the $H\alpha$ periodogram, however, and its value >100 days is far from either planet.

The ~ 15 -day signal associated with planet c is stable over the time baseline and across instruments, further suggesting a planetary explanation. Performing a two-planet fit (without a GP) on the CARMENES data, and doing the same with all data, yields consistent results ($K_{c,\text{carmenes}} = 3.20 \pm 0.58 \text{ m s}^{-1}$; $K_{c,\text{all}} = 3.18 \pm 0.49 \text{ m s}^{-1}$). Planetary signals are expected to remain stable over any observational baseline, while activity-sourced signals increase or decrease in amplitude over time. This analysis provides additional evidence for the true period of planet c at ~ 15 days. Performing the same analysis on the ~ 14 -day signal yields a noticeable decrease in amplitude with the new RV data

($K_{c,\text{carmenes}} = 2.64 \pm 0.63 \text{ m s}^{-1}$; $K_{c,\text{all}} = 2.38 \pm 0.52 \text{ m s}^{-1}$). While the two values are consistent, the 14-day signal appears more sensitive to the new data.

4.5. Joint Transit–RV Analysis

The final step of our analysis is the combination of the transit fits and RV fits into one complete, joint analysis. We adopt this model as our best, final model, as it is the most complete description of GJ 3929: it utilizes all data and characterizes both planets that are observed in this system, while also characterizing properties of planet b that can only be gleaned from photometry, especially its radius.

We performed a model comparison in Section 4.2, and we use that model comparison to select our preferred model, which is a two-planet model without the use of a GP. We performed this model comparison in the RV analysis rather than the joint analysis for one primary reason: all the free parameters of interest are primarily measured in the RVs. First, we were interested in deciding between a one- and two-planet model. The second planetary signal is *only* detected in the RVs; transit searches have been unsuccessful. Second, we wanted to differentiate between a 14- and 15-day period for planet c. Again, this signal is only represented in the RV data. Third, we wanted to justify the use of a GP. Our primary consideration for the use of a GP was in the RVs, as the photometries are quiet, as expected. A >100 -day rotation period would be unlikely to be observed in TESS PDCSAP flux, and the ground-based photometries are all far too short in baseline to be affected by a periodicity on even 1/100 of the rotation period’s timescale. Finally, we were interested in testing the veracity of eccentric models. Eccentricity, however, is much more strongly constrained by RVs than by photometry.

Our final, joint fit, then, was performed considering a two-planet model, where the second planet period is constrained between 15 and 16 days in order to prevent the MCMC chains from clustering around the alias at 14.2 days. The model is circular, and we do not adopt any GP to account for excess noise. We use the `exoplanet` software package in the joint fit, and the transits are modeled identically as described in Section 4.1. The RVs are modeled in `exoplanet` as well, with two Keplerian orbital solutions that model both photometric and RV data sets simultaneously. In particular, the period and time of conjunction of each planet are shared between the data sets, while other orbital parameters are typically constrained to one data set or another. A full list of the priors used in our model is available in Table 4.

We again use the HMC algorithm with a NUTS sampler for increased sampling efficiency. We again run 10,000 tuning steps and 10,000 subsequent posterior estimation steps. Our final transit fits are visible in Figure 4. Our final RV fit is visible in Figure 7. Finally, our posterior estimates for each model free parameter are listed in Table 5.

5. Discussion

We have refined the measured parameters for GJ 3929b ($P_b = 2.616235 \pm 0.000005$ days; $R_b = 1.09 \pm 0.04 R_{\oplus}$; $M_b = 1.75^{+0.44}_{-0.45} M_{\oplus}$; $\rho_b = 7.3 \pm 2.0 \text{ g cm}^{-3}$) and GJ 3929c ($P_c = 15.04 \pm 0.03$ days; $M \sin i_c = 5.71 \pm 0.94 M_{\oplus}$).

GJ 3929 joins a growing list of M-dwarf systems that contain a short-period terrestrial planet, accompanied by a nontransiting, more massive planet (i.e., Bonfils et al. 2018). Additionally, the

Table 4
Priors Used for Bayesian Model Fits

Parameter Name	Prior	Units	Description
Planet b Orbital Parameters			
P_b	$\mathcal{U}^a(2.0, 3.0)$	days	Period
$T_{\text{con},b}$	$\mathcal{U}(2459319.0, 2459320.0)$	BJD (days)	Time of inferior conjunction
$\sqrt{e} \cos \omega_b^*$	$\mathcal{U}(-1, 1)$...	Eccentricity reparameterization
$\sqrt{e} \sin \omega_b^*$	$\mathcal{U}(-1, 1)$...	Eccentricity reparameterization
$R_{p,b}/R_*$	$\log \mathcal{N}^b(0.0953, 1.0)$...	Scaled radius
b_b	$\mathcal{U}(0.0, 1.0)$...	Impact parameter
K_b	$\mathcal{U}(0.01, 100)$	m s^{-1}	Velocity semiamplitude
Planet c Orbital Parameters			
P_c	$\mathcal{U}(14.5, 16)$	days	Period
$T_{\text{con},c}$	$\mathcal{U}(2459064.0, 2459080.0)$	BJD (days)	Time of inferior conjunction
$\sqrt{e} \cos \omega_c^*$	$\mathcal{U}(-1, 1)$...	Eccentricity reparameterization
$\sqrt{e} \sin \omega_c^*$	$\mathcal{U}(-1, 1)$...	Eccentricity reparameterization
K_c	$\mathcal{U}(0.01, 100)$	m s^{-1}	Velocity semiamplitude
GP Hyperparameters			
η_1^*	$\mathcal{U}(0, 50)$	m s^{-1}	GP amplitude
η_2^*	$\mathcal{U}(0.1, 10, 000)$	days	Exponential decay length
η_3^*	$\mathcal{U}(100, 150)$	days	Recurrence rate (rotation period)
η_4^*	$\mathcal{U}(0.05, 0.6)$...	Periodic scale length
Instrumental Parameters			
γ_{CARMENES}	$\mathcal{U}(-100, 100)$	m s^{-1}	CARMENES systematic offset
γ_{NEID}	$\mathcal{U}(-100, 100)$	m s^{-1}	NEID systematic offset
γ_{HPF}	$\mathcal{U}(-100, 100)$	m s^{-1}	HPF systematic offset
σ_{CARMENES}	$\mathcal{U}(0.01, 100)$	m s^{-1}	CARMENES jitter
σ_{NEID}	$\mathcal{U}(0.01, 100)$	m s^{-1}	NEID jitter
σ_{HPF}	$\mathcal{U}(0.01, 100)$	m s^{-1}	HPF jitter
σ_{TESS}	$\log \mathcal{N}(-9.48, 2)$...	Photometric jitter
$\sigma_{\text{ARCTIC}-20210226}$	$\log \mathcal{N}(-9.67, 2)$...	Photometric jitter
$\sigma_{\text{ARCTIC}-20210430}$	$\log \mathcal{N}(-11.88, 2)$...	Photometric jitter
$\sigma_{\text{LCO}-\text{HAL}_{gp}}$	$\log \mathcal{N}(-12.41, 2)$...	Photometric jitter
$\sigma_{\text{LCO}-\text{HAL}_{ip}}$	$\log \mathcal{N}(-13.17, 2)$...	Photometric jitter
$\sigma_{\text{LCO}-\text{HAL}_{rp}}$	$\log \mathcal{N}(-12.96, 2)$...	Photometric jitter
$\sigma_{\text{LCO}-\text{HAL}_{rs}}$	$\log \mathcal{N}(-12.53, 2)$...	Photometric jitter
γ_{TESS}	$\mathcal{N}(0.0, 10.0)$...	Photometric offset
$\gamma_{\text{ARCTIC}-20210226}$	$\mathcal{N}(0.0, 10.0)$...	Photometric offset
$\gamma_{\text{ARCTIC}-20210430}$	$\mathcal{N}(0.0, 10.0)$...	Photometric offset
$\gamma_{\text{LCO}-\text{HAL}_{gp}}$	$\mathcal{N}(0.0, 10.0)$...	Photometric offset
$\gamma_{\text{LCO}-\text{HAL}_{ip}}$	$\mathcal{N}(0.0, 10.0)$...	Photometric offset
$\gamma_{\text{LCO}-\text{HAL}_{rp}}$	$\mathcal{N}(0.0, 10.0)$...	Photometric offset
$\gamma_{\text{LCO}-\text{HAL}_{rs}}$	$\mathcal{N}(0.0, 10.0)$...	Photometric offset
u_{TESS}	\mathcal{K}^c	...	Quadratic limb darkening
u_{ARCTIC}	\mathcal{K}	...	Quadratic limb darkening
$u_{\text{LCO}_{gp}}$	\mathcal{K}	...	Quadratic limb darkening
$u_{\text{LCO}_{ip}}$	\mathcal{K}	...	Quadratic limb darkening
$u_{\text{LCO}_{rp}}$	\mathcal{K}	...	Quadratic limb darkening
$u_{\text{LCO}_{rs}}$	\mathcal{K}	...	Quadratic limb darkening

Notes.^a \mathcal{U} is a uniform prior with $\mathcal{U}(\text{lower}, \text{upper})$.^b \mathcal{N} is a normal prior with $\mathcal{N}(\text{mean}, \text{standard deviation})$.^c \mathcal{K} is a reparameterization of a uniform prior for limb darkening, outlined in Kipping (2013).^d These parameters are not utilized in our final adopted fit. We include them for completeness.

possible existence of additional planetary companions cannot be ignored. M dwarfs in particular tend to have higher multiplicity of smaller exoplanets. Lu et al. (2020) used metallicity correlations when studying M-dwarf systems to estimate how

much planet-forming material is present in an initial planetary disk. It is likely that a correlation exists between metallicity of the host star and the amount of planet-forming material in a disk, especially for late-type stars (Bonfils et al. 2005;

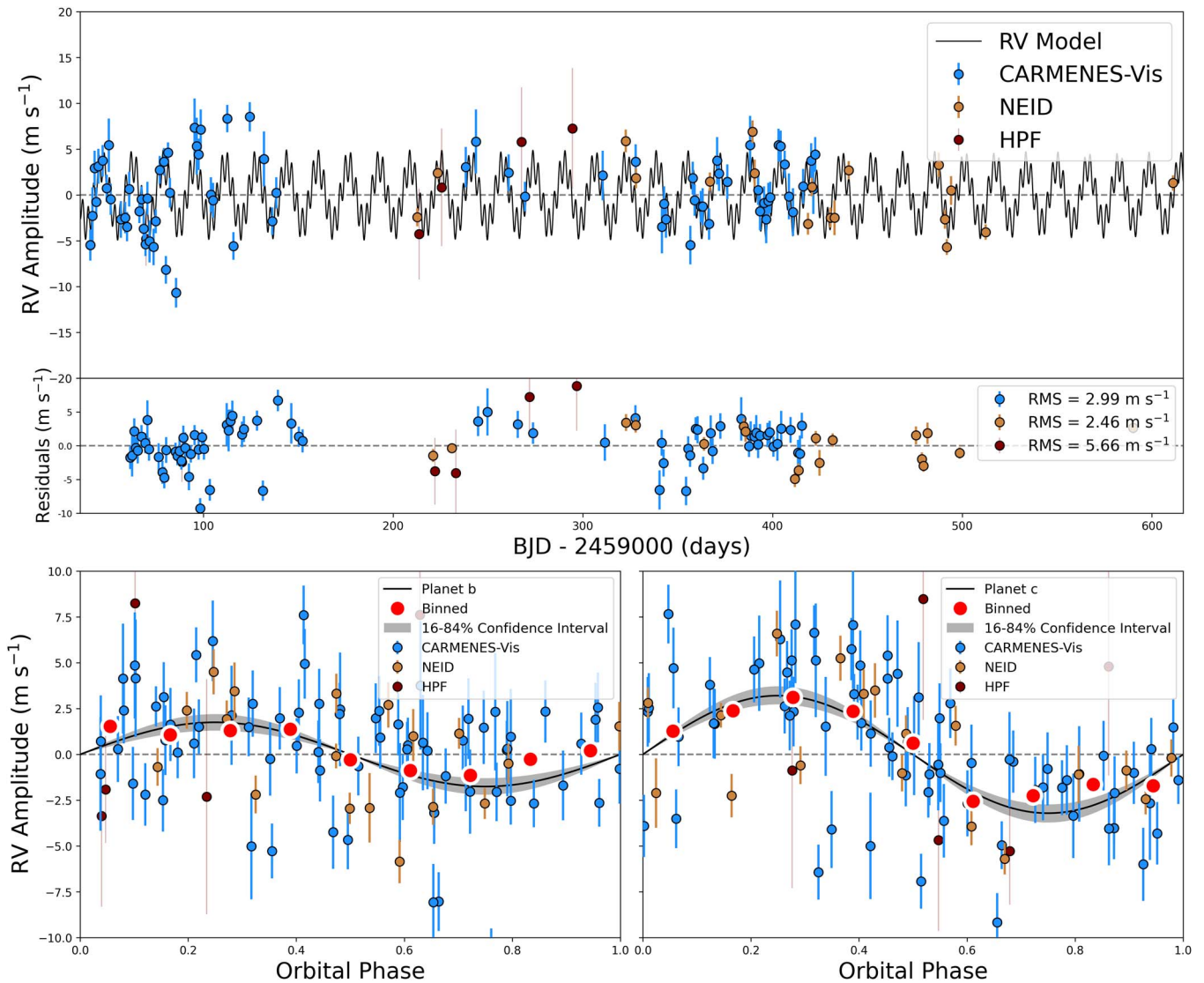


Figure 7. Top: RV data of GJ 3929 used in our analysis. The data have been adjusted for systematic offsets. Overlaid in black is the two-planet model. Bottom: phase folds of our median fit to planets b and c after subtracting the other planet, with a 1σ confidence interval overlaid. Jitter values are not included in the errors.

Johnson & Apps 2009). Lu et al. (2020) estimate only $9 M_{\oplus}$ of material for forming planets in a metal-poor ($[\text{Fe}/\text{H}] = -0.5$) early M dwarf ($M_* = 0.6 M_{\odot}$). While GJ 3929 is smaller ($M_* = 0.32 M_{\odot}$) than this system, its metallicity is much closer to the Sun ($[\text{Fe}/\text{H}] = -0.05$), giving it $\sim 15 M_{\oplus}$ of material to form planets, if we assume the disk-to-star mass ratio of 0.01 that Lu et al. (2020) adopt. The sum of the median mass of GJ 3929b ($1.75 M_{\oplus}$) and the median minimum mass of GJ 3929c ($5.70 M_{\oplus}$) are significantly less than this value, implying that planet c is significantly inclined and much more massive than we estimate, additional planets exist in the system, or the extra disk material was accreted onto the star.

We highlight the GJ 1132 system, characterized in Bonfils et al. (2018), for comparison with GJ 3929. GJ 1132b is also a short-period, Earth-sized rocky planet orbiting an M dwarf, with an additional nontransiting companion. GJ 3929b is denser than GJ 1132b, as seen in Figure 9, though its longer orbital period makes its RV semiamplitude a bit smaller. We include comparisons to this system further in the discussion to help frame GJ 3929 in the context of similar systems.

5.1. Planet b

GJ 3929b is an Earth-sized exoplanet, placing it below the radius gap for M dwarfs (Van Eylen et al. 2021; Petigura et al. 2022). Our mass and radius estimates allow us to constrain GJ 3929b’s bulk density and confirm its consistency with a composition slightly denser than Earth (Figure 9). Due to its proximity to its host star, GJ 3929b probably lost much of its atmosphere owing to X-ray and ultraviolet flux (Van Eylen et al. 2018). The addition of a nontransiting second planet in the system originally confounded our RV analysis of the system and further emphasizes the challenges discussed in He et al. (2021) relating to the mass measurement of transiting planets. Since more than half of the time the transiting planet in a system with nontransiting companions does not have the largest semiamplitude, initial follow-up can be confusing.

GJ 3929b is Venus-like ($S_b = 17.3^{+0.8}_{-0.7}$), in that it resides in its host star’s Venus zone. This is defined as the boundary between the runaway-greenhouse inner edge of the habitable zone (Kopparapu et al. 2013) and an orbital distance that would produce 25 times Earth-like flux (Ostberg & Kane 2019).

Table 5
Derived Parameters for Both Planets

Parameter	Units	GJ 3929b	GJ 3929c
Orbital Parameters:			
Orbital period	P (days)	2.616235 ± 0.000005	15.04 ± 0.03
Time of inferior conjunction	T_C (BJD _{TDB})	2458956.3962 ± 0.0005	2459070.9 ± 0.4
Eccentricity	e	0 (fixed)	0 (fixed)
Argument of periastron	ω (deg)	90 (fixed)	90 (fixed)
RV semiamplitude	K (m s ⁻¹)	$1.77^{+0.44}_{-0.45}$	3.22 ± 0.51
Transit Parameters:			
Scaled radius	R_p/R_*	0.0156 ± 0.0003	...
Scaled semimajor axis	a/R_*	16.8 ± 0.5	...
Impact parameter	b	$0.11^{+0.06}_{-0.07}$...
Orbital inclination	i (deg)	88.442 ± 0.008	...
Transit duration	T_{14} (days)	$0.0495^{+0.0008}_{-0.0007}$...
Planetary Parameters:			
Mass	M_p (M_\oplus)	$1.75^{+0.44}_{-0.45}$	$5.71^a \pm 0.94$
Radius	R_p (R_\oplus)	1.09 ± 0.04	...
Density	ρ_p (g cm ⁻³)	7.3 ± 2.0	...
Semimajor axis	a (AU)	0.0252 ± 0.0005	0.081 ± 0.002
Average incident flux	$\langle F \rangle$ (W m ⁻²)	$24,000 \pm 1000$	2300 ± 100
Planetary insolation	S (S_\oplus)	17.3 ± 0.7	1.68 ± 0.07
Equilibrium temperature ^b	T_{eq} (K)	568 ± 6	317 ± 3
Instrumental Parameters			
RV jitter	σ_{CARMENES} (m s ⁻¹)	1.80 ± 0.48	
	σ_{NEID} (m s ⁻¹)	2.25 ± 0.66	
	σ_{HPF} (m s ⁻¹)	6 ± 7	
RV offset	γ_{CARMENES} (m s ⁻¹)	0.97 ± 0.39	
	γ_{NEID} (m s ⁻¹)	5.56 ± 0.66	
	γ_{HPF} (m s ⁻¹)	8 ± 4	
Limb darkening	$u_{1,\text{TESS}}, u_{2,\text{TESS}}$	$0.3^{+0.3}_{-0.2}, 0.3 \pm 0.4$	
	$u_{1,\text{ARCTIC}}, u_{2,\text{ARCTIC}}$	$0.5 \pm 0.3, 0.0^{+0.4}_{-0.3}$	
	$u_{1,\text{LCO-HALgp}}, u_{2,\text{LCO-HALgp}}$	$1.0^{+0.5}_{-0.6}, -0.3^{+0.5}_{-0.4}$	
	$u_{1,\text{LCO-HALip}}, u_{2,\text{LCO-HALip}}$	$1.0^{+0.3}_{-0.4}, -0.3^{+0.4}_{-0.3}$	
	$u_{1,\text{LCO-HALtp}}, u_{2,\text{LCO-HALtp}}$	$0.3^{+0.3}_{-0.2}, 0.3 \pm 0.4$	
Photometric jitter	$u_{1,\text{LCO-HALzs}}, u_{2,\text{LCO-HALzs}}$	$0.3^{+0.3}_{-0.2}, 0.3 \pm 0.4$	
	σ_{TESS} (ppm)	10^{+14}_{-7}	
	$\sigma_{\text{ARCTIC-20210226}}$ (ppm)	514 ± 100	
	$\sigma_{\text{ARCTIC-20210430}}$ (ppm)	545 ± 60	
	$\sigma_{\text{LCO-HALgp}}$ (ppm)	4^{+33}_{-4}	
	$\sigma_{\text{LCO-HALip}}$ (ppm)	356 ± 42	
	$\sigma_{\text{LCO-HALtp}}$ (ppm)	558 ± 40	
	$\sigma_{\text{LCO-HALzs}}$ (ppm)	480 ± 40	
	mean _{TESS} (ppm)	40 ± 8	
	mean _{ARCTIC-20210226} (ppm)	400 ± 70	
mean _{ARCTIC-20210430} (ppm)	340 ± 60		
mean _{LCO-HALgp} (ppm)	350 ± 100		
mean _{LCO-HALip} (ppm)	360 ± 40		
mean _{LCO-HALtp} (ppm)	350 ± 40		
mean _{LCO-HALzs} (ppm)	340 ± 40		

Notes.^a Minimum mass.^b Estimated assuming an albedo of 0.

Learning more about planets in the Venus zone is an important step toward discovering Earth twins. Spectroscopic observations of the solar system, for example, would have a hard time distinguishing between Earth and Venus, despite their drastically different surface environments (Jordan et al. 2021). GJ 3929b is an excellent planet for studying the differences in spectra for a system that is Venus-like, and for which we are certain that it is nothing like Earth.

Fortunately, GJ 3929b is amenable to atmospheric study with the James Webb Space Telescope (JWST; Gardner et al. 2006). Beyond learning more about exo-Venuses, studying the atmosphere of GJ 3929b could help reveal the evolutionary history of the system and shed light on planet formation models. GJ 3929b has an estimated Transmission Spectroscopy Metric (TSM; Kempton et al. 2018) of 14 ± 4 , placing it in the top quintile of Earth-sized exoplanets amenable to JWST

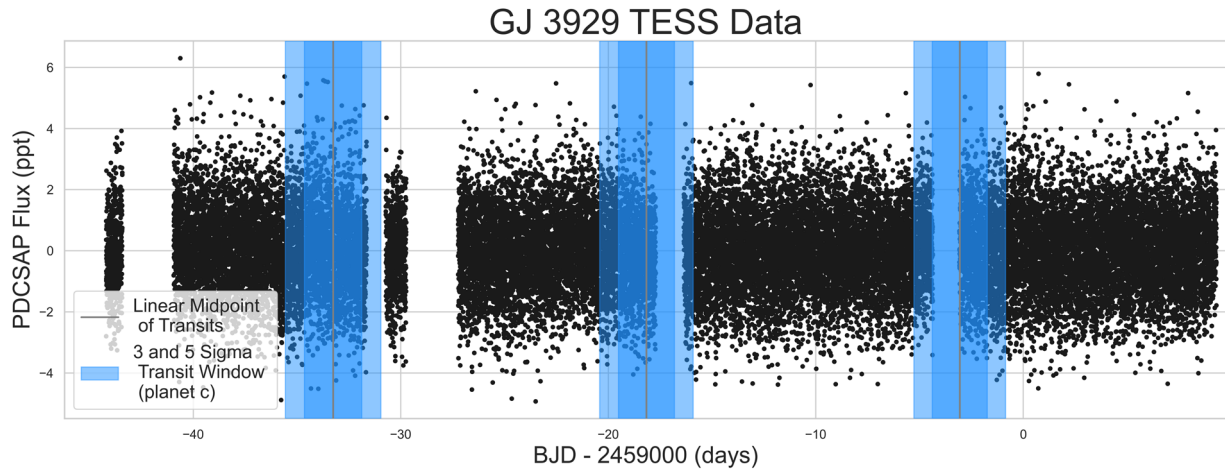


Figure 8. TESS PDCSAP flux of GJ 3929, taken during Sectors 24 and 25. The projected linear ephemeris of planet c is marked by a vertical gray line, with the 3σ and 5σ windows of uncertainty overlaid. It seems plausible that the second and third transits of planet c might have fallen into data gaps, though the negative detection in the first transit window cannot easily be explained if planet c is transiting. Thus, we can rule out transits of planet c with 3σ confidence.

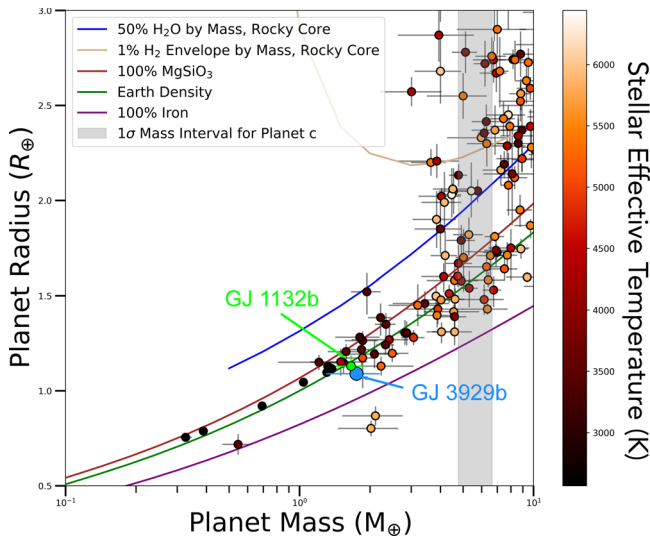


Figure 9. Mass–radius diagram of exoplanets taken from the NASA Exoplanet Archive on 2022 April 5. We restricted our study to planets with measured radii and masses. Colors indicate the stellar effective temperature of the system’s host star. GJ 3929b is depicted in blue, and a region spanning the possible positions of planet c is visible in gray. We also include GJ 1132b in green, as it is a similar system discussed further in the text. A few theoretical density estimates are included as outlined in Zeng et al. (2019).

observations. The density of GJ 3929b does not suggest a thick atmosphere, though a thin atmosphere of outgassed volatiles, a thin atmosphere lacking in volatiles and consisting of silicates and enriched in refractory elements, and a no-atmosphere scenario are all plausible (Seager & Deming 2010).

In Figure 10, we highlight GJ 3929b’s TSM in the context of other small exoplanets. We include all exoplanets with sufficient information to calculate a TSM on the NASA Exoplanet Archive, though we caution that only exoplanets with $>3\sigma$ mass measurements are likely to see follow-up with JWST owing to a degeneracy in the interpretation of spectra (Batalha et al. 2019). GJ 3929b occupies a truly rare position in this space, as quality mass measurements are very challenging for planets of its size, and small planets with mass measurements are usually not very amenable to transmission spectroscopy. We highlight a few other small planets amenable to transmission spectroscopy. Besides the TRAPPIST-1 system

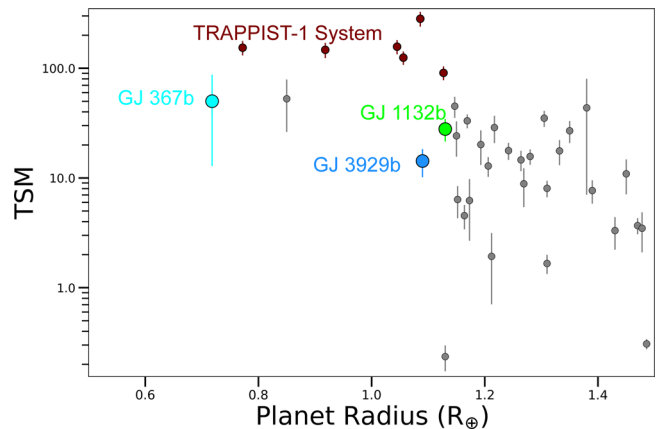


Figure 10. TSM (Kempton et al. 2018) of various planets taken from the NASA Exoplanet Archive on 2022 April 5. We note that GJ 3929b is in a sparsely populated region of parameter space, due largely to the difficulty of studying small exoplanets. We highlight a few other small-planet systems that are amenable to transmission spectroscopy.

(Agol et al. 2021), which is exceptional in most parameter spaces, few small planets are better for transmission spectroscopy than GJ 3929b. While GJ 1132b is a similar system to GJ 3929b and its TSM is slightly larger, GJ 3929b is brighter, making high-S/N measurements with JWST more likely, and making it more attractive for ground-based follow-up. On the other hand, GJ 367b is an ultra-short-period (USP) planet with a much higher TSM than GJ 3929b. However, its USP nature makes the existence of an atmosphere far less likely than for GJ 3929b, and further, any such atmosphere would likely exhibit very different chemistries from GJ 3929b, since its equilibrium temperature is more than 3 times hotter ($T_{\text{eq,GJ367b}} = 1745 \pm 43$ K; Lam et al. 2021).

5.2. Planet c

It is not clear whether or not GJ 3929c is a transiting exoplanet, though we detect no transits of this system in this study. Consequently, we cannot measure the radius of planet c, nor its bulk density.

The measured minimum mass of GJ 3929c suggests that it is at least a sub-Neptune in size when predicted from the mass–radius

relationship, and perhaps larger (Kanodia et al. 2019). M-dwarf systems consisting of a close-in, terrestrial exoplanet and longer-period sub-Neptunes are common occurrences (Rosenthal et al. 2021; Sabotta et al. 2021), though the brightness of GJ 3929 allows for a more detailed study than is often the case. GJ 3929 will not be observed by TESS during Cycle 5, though the success of the TESS mission suggests that it will likely continue for years longer. Additionally, the advent of future photometric missions (i.e., PLATO; Magrin et al. 2018) suggests that GJ 3929 will probably receive additional photometric observations in the future, and a transit of planet c may someday be identified.

5.3. Comparison to Kemmer et al. (2022)

The addition of HPF and NEID RV data, as well as diffuser-assisted ARCTIC data, have refined or changed various measured and derived parameters for each planet. Furthermore, our choice to use the ~ 15 -day signal as the period of GJ 3929c has an additional effect on several of the qualities of the planet.

The period and transit time of planet b are fully consistent with those found in Kemmer et al. (2022), though the uncertainty is slightly larger in our case. This is most likely due to Kemmer et al. (2022)’s use of more transit data and in general modeling more transits of planet b. We prioritized higher-precision photometry and consequently opted not to use the SAINT-EX photometry or the additional LCO data utilized in Kemmer et al. (2022). Furthermore, our team did not have access to the transits obtained by the Observatorio de Sierra Nevada (OSN). Our additional ARCTIC photometry changed the radius measurement from $1.150 \pm 0.04 R_{\oplus}$ to $1.09 \pm 0.04 R_{\oplus}$, though we note that these values are 1σ consistent.

The additional RVs did not shrink the formal 1σ error bars of the measured RV semi-amplitudes, but they did modify the mean posterior values, and the resulting K/σ of our mass measurements are improved. For planet b, Kemmer et al. (2022) found a mass of $1.21^{+0.40}_{-0.42} M_{\oplus}$, and we find a mass of $1.75^{+0.44}_{-0.45} M_{\oplus}$. Similarly for planet c, Kemmer et al. (2022) found a minimum mass of $5.27^{+0.74}_{-0.76} M_{\oplus}$, while we measure a minimum mass of $5.71 \pm 0.94 M_{\oplus}$. We note, however, that changing the period of planet c likely played a role in this change as well, not merely the additional RVs.

Perhaps the most significant departure from Kemmer et al. (2022) is that our final model did not utilize a GP. In fact, this is probably the most significant contribution to the increased mass uncertainties in our fits. When utilizing a GP, our model does yield more precise mass uncertainties than those in Kemmer et al. (2022), which is expected owing to our inclusion of additional data. The increased amplitudes remain, however, suggesting that their difference is not related to the use of a GP. As shown in Table 3, we cannot justify the use of a GP in our final fit.

6. Summary

We use RVs from the NEID, HPF, and CARMENES spectrographs to characterize the transiting planet GJ 3929b and the probably nontransiting planet GJ 3929c. We use diffuser-assisted photometry from the ARCTIC telescope in combination with LCOGT and TESS photometry in order to improve the radius of GJ 3929b ($R_b = 1.09 \pm 0.04 R_{\oplus}$), and we use RVs from CARMENES, NEID, and HPF to measure the mass of both planets ($M_b = 1.75 \pm 0.45 M_{\oplus}$; $M \sin i_c = 5.70 \pm 0.92 M_{\oplus}$). We conclude that GJ 3929 is a two-planet system with a

2.61626 ± 0.000005 -day transiting exo-Venus that is highly amenable to transmission spectroscopy. GJ 3929c is a more massive planet orbiting with a period of 15.04 ± 0.03 days that is unlikely to transit.

This paper includes data collected by the TESS mission. Funding for the TESS mission is provided by NASA’s Science Mission Directorate.

The Hobby–Eberly Telescope (HET) is a joint project of the University of Texas at Austin, the Pennsylvania State University, Ludwig-Maximilians-Universität München, and Georg-August-Universität Göttingen. The HET is named in honor of its principal benefactors, William P. Hobby and Robert E. Eberly.

The authors thank the HET Resident Astronomers for executing the observations included in this manuscript.

We would like to acknowledge that the HET is built on Indigenous land. Moreover, we would like to acknowledge and pay our respects to the Carrizo & Comecrudo, Coahuiltecan, Caddo, Tonkawa, Comanche, Lipan Apache, Alabama-Coushatta, Kickapoo, Tigua Pueblo, and all the American Indian and Indigenous Peoples and communities who have been or have become a part of these lands and territories in Texas, here on Turtle Island.

These results are based on observations obtained with the Habitable-zone Planet Finder Spectrograph on the HET. The HPF team was supported by NSF grants AST-1006676, AST-1126413, AST-1310885, AST-1517592, AST-1310875, AST-1910954, AST-1907622, AST-1909506, ATI 2009889, ATI-2009982, AST-2108512, AST-2108801, AST-2108493, and AST-2108569 and the NASA Astrobiology Institute (NNA09DA76A) in the pursuit of precision RVs in the NIR. The HPF team was also supported by the Heising-Simons Foundation via grant 2017-0494. This project was also supported by NSF grant AST-1909682.

Based on observations at Kitt Peak National Observatory, NSF’s NOIRLab (Prop. ID 2020B-0422; PI: A. Lin. Prop. ID 2021A-0385; PI: A. Lin. Prop. ID 2021B-0435; PI: S. Kanodia. Prop ID 2021B-0035; PI: S. Kanodia), managed by the Association of Universities for Research in Astronomy (AURA) under a cooperative agreement with the National Science Foundation. The authors are honored to be permitted to conduct astronomical research on Iolkam Du’ag (Kitt Peak), a mountain with particular significance to the Tohono O’odham.

This paper contains data taken with the NEID instrument, which was funded by the NASA-NSF Exoplanet Observational Research (NN-EXPLORE) partnership and built by Pennsylvania State University. NEID is installed on the WIYN telescope, which is operated by the NSF’s National Optical-Infrared Astronomy Research Laboratory (NOIRLab), and the NEID archive is operated by the NASA Exoplanet Science Institute at the California Institute of Technology. NN-EXPLORE is managed by the Jet Propulsion Laboratory, California Institute of Technology, under contract with the National Aeronautics and Space Administration.

We thank the NEID Queue Observers and WIYN Observing Associates for their skillful execution of our NEID observations.

This work was partially supported by funding from the Center for Exoplanets and Habitable Worlds. The Center for Exoplanets and Habitable Worlds is supported by the Pennsylvania State University and the Eberly College of Science.

This research was supported in part by a Seed Grant award from the Institute for Computational and Data Sciences at the Pennsylvania State University.

This work has made use of data from the European Space Agency (ESA) mission Gaia (<https://www.cosmos.esa.int/gaia>), processed by the Gaia Data Processing and Analysis Consortium (DPAC, <https://www.cosmos.esa.int/web/gaia/dpac/consortium>). Funding for the DPAC has been provided by national institutions, in particular the institutions participating in the Gaia Multilateral Agreement.

This research made use of `exoplanet` (Foreman-Mackey et al. 2021a, 2021b) and its dependencies (Astropy Collaboration et al. 2013; Kipping 2013; Salvatier et al. 2016; Theano Development Team 2016; Foreman-Mackey et al. 2017; Foreman-Mackey 2018; Astropy Collaboration et al. 2018; Luger et al. 2019; Kumar et al. 2019; Agol et al. 2020).

This research made use of `Lightkurve`, a Python package for Kepler and TESS data analysis (Lightkurve Collaboration, 2018).

This research has made use of the SIMBAD database, operated at CDS, Strasbourg, France.

This research has made use of the NASA Exoplanet Archive, which is operated by the California Institute of Technology, under contract with the National Aeronautics and Space Administration under the Exoplanet Exploration Program.

This research has made use of the Exoplanet Follow-up Observation Program (ExoFOP; DOI: 10.26134/ExoFOP5) website, which is operated by the California Institute of Technology, under contract with the National Aeronautics and Space Administration under the Exoplanet Exploration Program.

This research was, in part, carried out at the Jet Propulsion Laboratory, California Institute of Technology, under a contract with the National Aeronautics and Space Administration (80NM0018D0004).

C.I.C. acknowledges support by NASA Headquarters under the NASA Earth and Space Science Fellowship Program through grant 80NSSC18K1114.

Facilities: Gaia, HET (HPF), TESS, RBO, APO (ARCTIC), WIYN (NEID), Shane (ShARCS), Exoplanet Archive.

Software: `ArviZ` (Kumar et al. 2019), `AstroImageJ` (Collins et al. 2017), `astropy` (Astropy Collaboration et al. 2018), `barycorrpy` (Kanodia & Wright 2018), `exoplanet` (Foreman-Mackey et al. 2021b), `ipython` (Pérez & Granger 2007), `lightkurve` (Lightkurve Collaboration et al. 2018), `matplotlib` (Hunter 2007), `numpy` (Harris et al. 2020), `pandas` (pandas development team 2020; Wes McKinney 2010), `PyMC3` (Salvatier et al. 2016), `RadVel` (Fulton et al. 2018), `scipy` (Virtanen et al. 2020), `SERVAL` (Zechmeister et al. 2018), `starry` (Luger et al. 2019), `Theano` (Theano Development Team 2016), `TransitLeastSquares` (Hippke & Heller 2019).

Appendix

We include the RV data taken by our team (Tables 6 and 7). We include a corner plot of a few of our model parameters in Figure 11.

Table 6
NEID RVs of GJ 3929

BJD _{TDB} (days)	RV (m s ⁻¹)	σ (m s ⁻¹)	S/N ₁₀₂	H α Index	σ H α Index
2,459,221.0168	7.4	1.8	29.41	0.971	0.007
2,459,221.0275	1.66	1.63	32.04	0.973	0.006
2,459,221.0384	1.05	1.69	31.09	0.965	0.006
2,459,231.0107	4.72	10.47	5.51	1.049	0.046
2,459,231.0167	8.66	1.16	43.58	0.956	0.004
2,459,231.0274	6.81	1.29	40.16	0.956	0.005
2,459,231.0382	8.31	1.09	46.21	0.956	0.004
2,459,322.8407	11.47	1.24	43.41	0.939	0.004
2,459,327.8212	7.42	1.08	49.62	0.941	0.004
2,459,363.9174	7.05	1.01	51.56	0.946	0.004
2,459,384.7824	12.5	1.23	42.22	0.947	0.004
2,459,385.7494	7.97	1.48	36.59	0.957	0.005
2,459,411.8444	2.45	1.18	44.79	0.944	0.004
2,459,413.763	6.47	1.03	48.56	0.926	0.004
2,459,422.8348	3.12	1.09	47.69	0.935	0.004
2,459,424.7787	3.12	1.9	27.83	0.93	0.007
2,459,431.7429	8.28	1.0	50.77	0.93	0.003
2,459,434.7056	-0.66	1.25	41.15	0.942	0.004
2,459,475.6962	8.87	1.33	37.61	0.965	0.005
2,459,478.6923	2.94	1.02	48.36	0.954	0.004
2,459,479.6223	-0.1	0.85	54.55	0.947	0.003
2,459,481.6797	6.08	1.57	31.97	0.957	0.006
2,459,498.5889	1.54	0.84	56.35	0.953	0.003
2,459,590.0301	6.89	0.86	54.54	0.945	0.003

Note. We do not include the five NEID RVs with failed drift solutions.

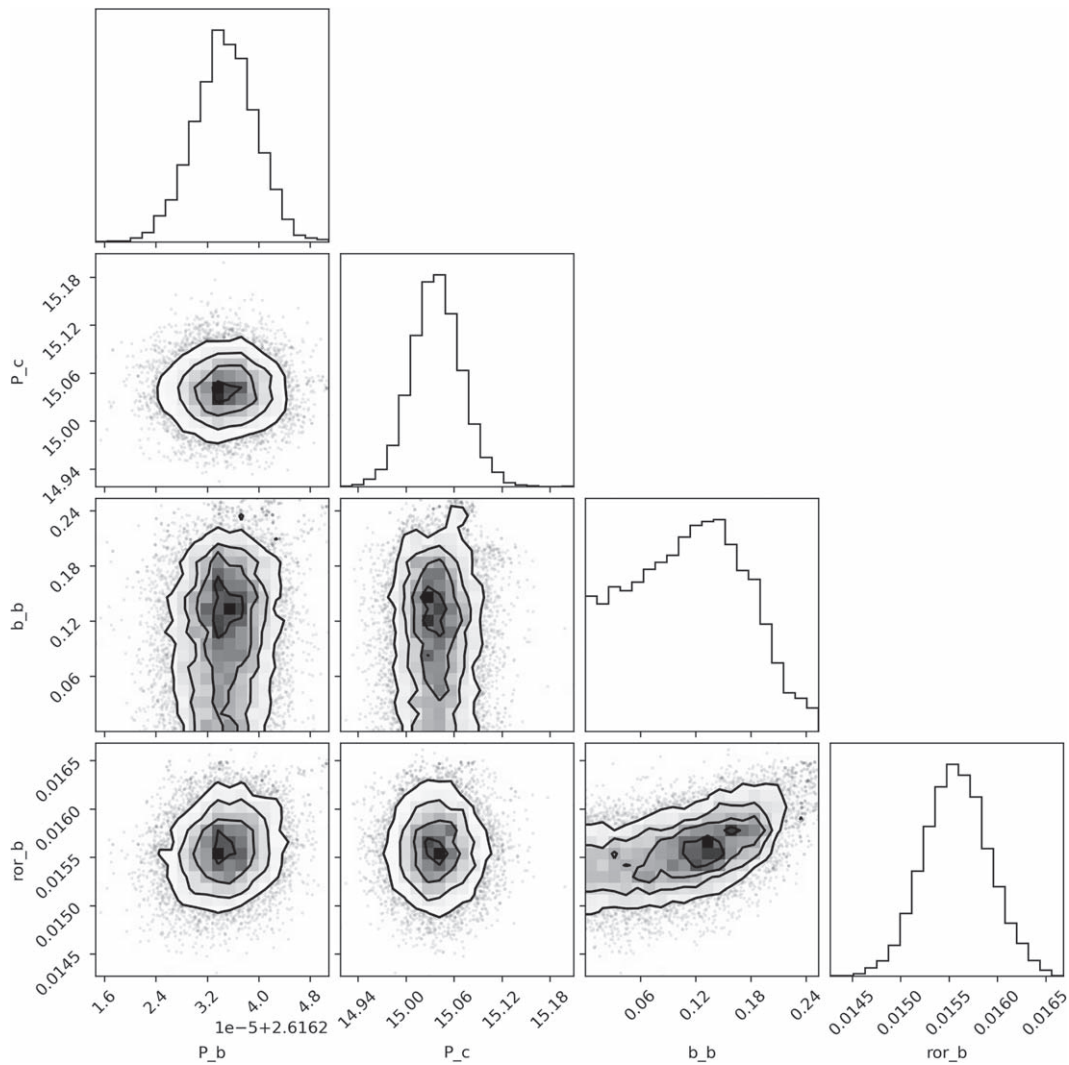


Figure 11. We include a corner plot of a few key parameters generated during our joint fit. At the top of each column is a histogram of each parameter’s values during the MCMC process, marginalized over other parameters.

Table 7
HPF RVs of GJ 3929

BJD _{TDB} (days)	RV (m s ⁻¹)	σ (m s ⁻¹)	S/N ₁₈
2,459,088.6272	-16.43	4.98	210.68
2,459,088.6349	-5.87	4.84	214.31
2,459,088.6426	-3.77	5.17	202.62
2,459,222.0314	-3.74	5.48	189.58
2,459,222.0392	1.12	5.03	206.82
2,459,222.0470	-4.42	5.05	207.29
2,459,233.0037	1.42	7.62	135.48
2,459,233.0117	6.38	7.79	133.86
2,459,233.0195	12.04	7.54	140.42
2,459,271.8998	20.83	6.97	151.17
2,459,271.9076	4.8	6.51	162.75
2,459,271.9154	3.63	7.21	146.2
2,459,296.8246	9.54	9.38	114.91
2,459,296.8327	0.5	7.96	136.29
2,459,296.8403	6.47	7.1	147.33
2,459,649.8572	-14.68	13.81	82.09
2,459,649.8652	8.43	13.75	83.03
2,459,649.8719	4.25	25.37	49.05

ORCID iDs

Corey Beard  <https://orcid.org/0000-0001-7708-2364>
 Paul Robertson  <https://orcid.org/0000-0003-0149-9678>
 Shubham Kanodia  <https://orcid.org/0000-0001-8401-4300>
 Jack Lubin  <https://orcid.org/0000-0001-8342-7736>
 Caleb I. Cañas  <https://orcid.org/0000-0003-4835-0619>
 Arvind F. Gupta  <https://orcid.org/0000-0002-5463-9980>
 Rae Holcomb  <https://orcid.org/0000-0002-5034-9476>
 Sinclair Jones  <https://orcid.org/0000-0002-7227-2334>
 Jessica E. Libby-Roberts  <https://orcid.org/0000-0002-2990-7613>
 Andrea S. J. Lin  <https://orcid.org/0000-0002-9082-6337>
 Suvrath Mahadevan  <https://orcid.org/0000-0001-9596-7983>
 Guðmundur Stefánsson  <https://orcid.org/0000-0001-7409-5688>
 Chad F. Bender  <https://orcid.org/0000-0003-4384-7220>
 Cullen H. Blake  <https://orcid.org/0000-0002-6096-1749>
 William D. Cochran  <https://orcid.org/0000-0001-9662-3496>
 Michael Endl  <https://orcid.org/0000-0002-7714-6310>
 Mark Everett  <https://orcid.org/0000-0002-0885-7215>
 Eric B. Ford  <https://orcid.org/0000-0001-6545-639X>
 Connor Fredrick  <https://orcid.org/0000-0002-0560-1433>
 Samuel Halverson  <https://orcid.org/0000-0003-1312-9391>
 Leslie Hebb  <https://orcid.org/0000-0003-1263-8637>
 Dan Li  <https://orcid.org/0000-0001-7318-6318>
 Sarah E. Logsdon  <https://orcid.org/0000-0002-9632-9382>
 Jacob Luhn  <https://orcid.org/0000-0002-4927-9925>
 Michael W. McElwain  <https://orcid.org/0000-0003-0241-8956>
 Andrew J. Metcalf  <https://orcid.org/0000-0001-5000-1018>
 Joe P. Ninan  <https://orcid.org/0000-0001-8720-5612>
 Jayadev Rajagopal  <https://orcid.org/0000-0002-2488-7123>
 Arpita Roy  <https://orcid.org/0000-0001-8127-5775>
 Maria Schutte  <https://orcid.org/0000-0003-2435-130X>
 Christian Schwab  <https://orcid.org/0000-0002-4046-987X>
 Ryan C. Terrien  <https://orcid.org/0000-0002-4788-8858>
 John Wisniewski  <https://orcid.org/0000-0001-9209-1808>
 Jason T. Wright  <https://orcid.org/0000-0001-6160-5888>

References

- Agol, E., Dorn, C., Grimm, S. L., et al. 2021, *PSJ*, 2, 1
 Agol, E., Luger, R., & Foreman-Mackey, D. 2020, *AJ*, 159, 123
 Allard, F., Homeier, D., & Freytag, B. 2012, *RSPTA*, 370, 2765
 Ambikasaran, S., Foreman-Mackey, D., Greengard, L., Hogg, D. W., & O’Neil, M. 2015, *ITPAM*, 38, 252
 Anglada-Escudé, G., Arriagada, P., Vogt, S. S., et al. 2012, *ApJL*, 751, L16
 Astropy Collaboration, Price-Whelan, A. M., Sipőcz, B. M., et al. 2018, *AJ*, 156, 123
 Astropy Collaboration, Robitaille, T. P., Tollerud, E. J., et al. 2013, *A&A*, 558, A33
 Bailer-Jones, C. A. L., Rybizki, J., Foesneau, M., Demleitner, M., & Andrae, R. 2021, *AJ*, 161, 147
 Bailer-Jones, C. A. L., Rybizki, J., Foesneau, M., Mantelet, G., & Andrae, R. 2018, *AJ*, 156, 58
 Bakos, G., Noyes, R. W., Kovács, G., et al. 2004, *PASP*, 116, 266
 Baranne, A., Queloz, D., Mayor, M., et al. 1996, *A&AS*, 119, 373
 Batalha, N. E., Lewis, T., Fortney, J. J., et al. 2019, *ApJL*, 885, L25
 Beard, C., Robertson, P., Kanodia, S., et al. 2022, *AJ*, 163, 286
 Bonfils, X., Almenara, J. M., Cloutier, R., et al. 2018, *A&A*, 618, A142
 Bonfils, X., Delfosse, X., Udry, S., et al. 2005, *A&A*, 442, 635
 Borucki, W. J., Koch, D., Basri, G., et al. 2010, *Sci*, 327, 977
 Brown, T. M., Baliber, N., Bianco, F. B., et al. 2013, *PASP*, 125, 1031
 Cañas, C. I., Mahadevan, S., Cochran, W. D., et al. 2022, *AJ*, 163, 3
 Clough, S. A., Shephard, M. W., Mlawer, E. J., et al. 2005, *JQSR*, 91, 233
 Collins, K. A., Kielkopf, J. F., Stassun, K. G., & Hessman, F. V. 2017, *AJ*, 153, 77
 Colomé, J., Casteels, K., Ribas, I., & Francisco, X. 2010, *Proc. SPIE*, 7740, 77403K
 Cutri, R. M., Skrutskie, M. F., van Dyk, S., et al. 2003, 2MASS All Sky Catalog of Point Sources
 Danby, J. M. A. 1988, *Fundamentals of Celestial Mechanics* (Richmond, VA: Willmann-Bell)
 Dressing, C. D., & Charbonneau, D. 2015, *ApJ*, 807, 45
 Eastman, J., Gaudi, B. S., & Agol, E. 2013, *PASP*, 125, 83
 Espinoza, N., Bayliss, D., Hartman, J. D., et al. 2016, *AJ*, 152, 108
 Feinstein, A. D., Montet, B. T., Foreman-Mackey, D., et al. 2019, *PASP*, 131, 094502
 Fitzpatrick, E. L. 1999, *PASP*, 111, 63
 Ford, E. B. 2006, *ApJ*, 642, 505
 Foreman-Mackey, D. 2018, *RNAAS*, 2, 31
 Foreman-Mackey, D., Agol, E., Ambikasaran, S., & Angus, R. 2017, *AJ*, 154, 220
 Foreman-Mackey, D., Hogg, D. W., Lang, D., & Goodman, J. 2013, *PASP*, 125, 306
 Foreman-Mackey, D., Luger, R., Agol, E., et al. 2021a, exoplanet: Gradient-based probabilistic inference for exoplanet data & other astronomical time series, Zenodo, doi: 10.5281/zenodo.1998447
 Foreman-Mackey, D., Savel, A., Luger, R., et al. 2021b, exoplanet-dev/exoplanet v0.5.1, doi:10.5281/zenodo.1998447
 Fulton, B. J., Petigura, E. A., Blunt, S., & Sinukoff, E. 2018, *PASP*, 130, 044504
 Gaia Collaboration, Brown, A. G. A., Vallenari, A., et al. 2018, *A&A*, 616, A1
 Gaia Collaboration, Brown, A. G. A., Vallenari, A., et al. 2021, *A&A*, 649, A1
 Gaia Collaboration, Prusti, T., de Bruijne, J. H. J., et al. 2016, *A&A*, 595, A1
 Gardner, J. P., Mather, J. C., Clampin, M., et al. 2006, *SSRv*, 123, 485
 Gray, D. F., Baliunas, S. L., Lockwood, G. W., & Skiff, B. A. 1992, *ApJ*, 400, 681
 Green, G. M., Schlafly, E., Zucker, C., Speagle, J. S., & Finkbeiner, D. 2019, *ApJ*, 887, 93
 Gullikson, K., Dodson-Robinson, S., & Kraus, A. 2014, *AJ*, 148, 53
 Harris, C. R., Millman, K. J., van der Walt, S. J., et al. 2020, *Natur*, 585, 357
 Haywood, R. D., Collier Cameron, A., Queloz, D., et al. 2014, *MNRAS*, 443, 2517
 He, M. Y., Ford, E. B., & Ragozzine, D. 2021, *AJ*, 162, 216
 Hippke, M., & Heller, R. 2019, *A&A*, 623, A39
 Hoffman, M. D., & Gelman, A. 2011, arXiv:1111.4246
 Hornum, F., Hippler, S., Brandner, W., Wagner, K., & Henning, T. 2008, *Proc. SPIE*, 7014, 701448
 Huehnerhoff, J., Ketzbeck, W., Bradley, A., et al. 2016, *Proc. SPIE*, 9908, 99085H
 Hunter, J. D. 2007, *CSE*, 9, 90
 Hurvich, C. M., & Tsai, C.-L. 1993, *J. Time Ser. Anal.*, 14, 271
 Jenkins, J. M., Twicken, J. D., McCauliff, S., et al. 2016, *Proc. SPIE*, 9913, 99133E
 Johnson, J. A., & Apps, K. 2009, *ApJ*, 699, 933
 Jordan, S., Rimmer, P. B., Shorttle, O., & Constantinou, T. 2021, *ApJ*, 922, 44
 Kanodia, S., Mahadevan, S., Ramsey, L. W., et al. 2018, *Proc. SPIE*, 10702, 107026Q
 Kanodia, S., Stefansson, G., Cañas, C. I., et al. 2021, *AJ*, 162, 135
 Kanodia, S., Wolfgang, A., Stefansson, G. K., Ning, B., & Mahadevan, S. 2019, *ApJ*, 882, 38
 Kanodia, S., & Wright, J. 2018, *RNAAS*, 2, 4
 Kass, R. E., & Raftery, A. E. 1995, *J. Am. Stat. Assoc.*, 90, 773
 Kemmer, J., Dreizler, S., Kossakowski, D., et al. 2022, *A&A*, 659, A17
 Kempton, E. M. R., Bean, J. L., Louie, D. R., et al. 2018, *PASP*, 130, 114401
 Kipping, D. M. 2013, *MNRAS*, 435, 2152
 Kopparapu, R. K., Ramirez, R., Kasting, J. F., et al. 2013, *ApJ*, 765, 131
 Kossakowski, D., Kemmer, J., Bluhm, P., et al. 2021, *A&A*, 656, A124
 Kovács, G., Zucker, S., & Mazeh, T. 2002, *A&A*, 391, 369
 Kumar, R., Carroll, C., Hartikainen, A., & Martin, O. 2019, *JOSS*, 4, 1143
 Lam, K. W. F., Csizmadia, S., Astudillo-Defru, N., et al. 2021, *Sci*, 374, 1271
 Lightkurve Collaboration, Cardoso, J. V. d. M., Hedges, C., et al. 2018, Lightkurve: Kepler and TESS time Series Analysis in Python, Astrophysics Source Code Library, ascl:1812.013
 Lindgren, L., & Dravins, D. 2021, *A&A*, 652, A45
 Livingston, J. H., Endl, M., Dai, F., et al. 2018, *AJ*, 156, 78
 López-Morales, M., Haywood, R. D., Coughlin, J. L., et al. 2016, *AJ*, 152, 204
 Lu, C. X., Schlauffman, K. C., & Cheng, S. 2020, *AJ*, 160, 253
 Lubin, J., Robertson, P., Stefansson, G., et al. 2021, *AJ*, 162, 61
 Lubin, J., Van Zandt, J., Holcomb, R., et al. 2022, *AJ*, 163, 101
 Luger, R., Agol, E., Foreman-Mackey, D., et al. 2019, *AJ*, 157, 64
 Magrin, D., Ragazzoni, R., Rauer, H., et al. 2018, *Proc. SPIE*, 10698, 106984X

- Mahadevan, S., Ramsey, L., Bender, C., et al. 2012, *Proc. SPIE*, 8446, 84461S
- Mahadevan, S., Ramsey, L. W., Terrien, R., et al. 2014, *Proc. SPIE*, 9147, 91471G
- Mann, A. W., Feiden, G. A., Gaidos, E., Boyajian, T., & von Braun, K. 2015, *ApJ*, 804, 64
- McCully, C., Volgenau, N. H., Harbeck, D.-R., et al. 2018, *Proc. SPIE*, 10707, 107070K
- McKinney, W. 2010, in Proc. of the 9th Python in Science Conf., 445 (Austin, TX: SciPy), 56
- Narita, N., Fukui, A., Yamamuro, T., et al. 2020, *Proc. SPIE*, 11447, 114475K
- Ostberg, C., & Kane, S. R. 2019, *AJ*, 158, 195
- pandas development team 2020, pandas-dev/pandas: Pandas, v1.4.2, Zenodo, doi:10.5281/zenodo.3509134
- Pérez, F., & Granger, B. E. 2007, *CSE*, 9, 21
- Petigura, E. A., Rogers, J. G., Isaacson, H., et al. 2022, *AJ*, 163, 179
- Powell, M. J. D. 1998, *AcNum*, 7, 287
- Quirrenbach, A., Amado, P. J., Caballero, J. A., et al. 2014, *Proc. SPIE*, 9147, 91471F
- Ricker, G. R., Winn, J. N., Vanderspek, R., et al. 2015, *JATIS*, 1, 014003
- Robertson, P., Anderson, T., Stefansson, G., et al. 2019, *JATIS*, 5, 015003
- Rosenthal, L. J., Fulton, B. J., Hirsch, L. A., et al. 2021, *ApJS*, 255, 8
- Sabotta, S., Schlecker, M., Chaturvedi, P., et al. 2021, *A&A*, 653, A114
- Salvatier, J., Wiecki, T. V., & Fonnesbeck, C. 2016, *PeerJ Comp. Sci.*, 2, e55
- Schwab, C., Rakich, A., Gong, Q., et al. 2016, *Proc. SPIE*, 9908, 99087H
- Seager, S., & Deming, D. 2010, *ARA&A*, 48, 631
- Shappee, B., Prieto, J., Stanek, K. Z., et al. 2014, AAS Meeting Abstracts, 223, 236.03
- Shetrone, M., Cornell, M. E., Fowler, J. R., et al. 2007, *PASP*, 119, 556
- Siverd, R. J., Beatty, T. G., Pepper, J., et al. 2012, *ApJ*, 761, 123
- Srinath, S., McGurk, R., Rockosi, C., et al. 2014, *Proc. SPIE*, 9148, 91482Z
- Stassun, K. G., Oelkers, R. J., Pepper, J., et al. 2018, *AJ*, 156, 102
- Stassun, K. G., Oelkers, R. J., Paegert, M., et al. 2019, *AJ*, 158, 138
- Stefánsson, G., Cañas, C., Wisniewski, J., et al. 2020, *AJ*, 159, 100
- Stefansson, G., Hearty, F., Robertson, P., et al. 2016, *ApJ*, 833, 175
- Stefansson, G., Mahadevan, S., Hebb, L., et al. 2017, *ApJ*, 848, 9
- Stefansson, G., Mahadevan, S., Petrovich, C., et al. 2021, *ApJL*, 931, 16
- Stefansson, G., Mahadevan, S., Wisniewski, J., et al. 2018, *Proc. SPIE*, 10702, 1518
- Stumpe, M. C., Smith, J. C., Van Cleve, J. E., et al. 2012, *PASP*, 124, 985
- Theano Development Team 2016, arXiv:1605.02688
- Van Eylen, V., Agentoft, C., Lundkvist, M. S., et al. 2018, *MNRAS*, 479, 4786
- Van Eylen, V., Astudillo-Defru, N., Bonfils, X., et al. 2021, *MNRAS*, 507, 2154
- Virtanen, P., Gommers, R., Oliphant, T. E., et al. 2020, *NatMe*, 17, 261
- Weiss, L. M., Dai, F., Huber, D., et al. 2021, *AJ*, 161, 56
- Wright, E. L., Eisenhardt, P. R. M., Mainzer, A. K., et al. 2010, *AJ*, 140, 1868
- Yee, S. W., Petigura, E. A., & von Braun, K. 2017, *ApJ*, 836, 77
- Zechmeister, M., & Kürster, M. 2009, *A&A*, 496, 577
- Zechmeister, M., Reiners, A., Amado, P. J., et al. 2018, *A&A*, 609, A12
- Zeng, L., Jacobsen, S. B., Sasselov, D. D., et al. 2019, *PNAS*, 116, 9723